Proposal for All-Electrical Skyrmion Detection in van der Waals Tunnel Junctions

Dongzhe Li, Soumyajyoti Haldar, Stefan Heinze

Proposal for all-electrical skyrmion detection in van der Waals tunnel junctions

Dongzhe Li,*,† Soumyajyoti Haldar,*,‡ and Stefan Heinze‡

†*CEMES, Université de Toulouse, CNRS, 29 rue Jeanne Marvig, F-31055 Toulouse, France*
‡*Institute of Theoretical Physics and Astrophysics, University of Kiel, Leibnizstrasse 15, 24098 Kiel, Germany*
¶*Kiel Nano, Surface, Interface Science (KiNSIS), University of Kiel, 24118 Kiel, Germany*

E-mail: dongzhe.li@cemes.fr; haldar@physik.uni-kiel.de

Abstract

A major challenge for magnetic skyrmions in atomically thin van der Waals (vdW) materials is reliable skyrmion detection. Here, based on rigorous first-principles calculations, we show that all-electrical skyrmion detection is feasible in 2D vdW magnets via scanning tunneling microscopy (STM) and in planar tunnel junctions. We use the nonequilibrium Green's function method for quantum transport in planar junctions, including self-energy due to electrodes and working conditions, going beyond the standard Tersoff-Hamann approximation. We obtain a very large tunneling anisotropic magnetoresistance (TAMR) around the Fermi energy for a vdW tunnel junction based on graphite/Fe_3GeTe_2/germanene/graphite. For atomic-scale skyrmions the noncollinear magnetoresistance (NCMR) reaches giant values. We trace the origin of the NCMR to spin-mixing between spin-up and -down states of p_z and d_{z^2} character at the surface atoms. Both TAMR and NCMR are drastically enhanced in tunnel junctions with respect to STM geometry due to orbital symmetry matching at the interface.

Keywords: Spintronics, Magnetic skyrmions, Quantum transport, Noncollinear magnetoresistance, van der Waals tunnel junctions

Magnetic skyrmions[1] – topologically stabilized chiral spin structures with size down to the nanometer scale – have emerged as a promising avenue to realize next-generation spintronic devices.[2–4] Ten years ago, Fert and co-workers first proposed to use skyrmions in a race-track memory in their seminal paper.[5] Today, many other potential applications of skyrmions are being explored ranging from logic devices to neuromorphic or quantum computing.[6–9] An essential prerequisite for most applications is reliable electrical detection of individual skyrmions or other topological spin structures.

In ultrathin transition-metal films, skyrmions have been observed directly using spin-polarized scanning tunneling microscopy (STM),[10,11] which is based on the tunneling magnetoresistance (TMR). TMR devices rely on magnetic electrodes, which may perturb the skyrmion state during detection. Skyrmion detection is also possible via the tunneling anisotropic magnetoresistance (TAMR)[12,13] using non-magnetic STM tips.[10,14,15] However, because TAMR relies purely on spin-orbit coupling (SOC), it is typically too small for device applications. In 2015, the noncollinear magnetoresistance (NCMR) has been discovered and proposed for skyrmion detection.[16] NCMR is based on spin-mixing of majority and minority spin channels in a non-collinear spin structure.[16–19] Since it is not caused by SOC, it can be much larger than TAMR. In STM experiments, the NCMR can be used to observe skyrmions as well as domain walls.[16,19,20]

An alternative way for all-electrical skyrmion

detection is to use the topological Hall effect.[21–24] However, such device setups are more difficult to fabricate in terms of device geometries. A simpler solution is to design perpendicular tunnel junctions that can easily integrate skyrmions into conventional semiconductor devices, e.g., magnetic tunnel junctions (MTJ) for skyrmions.[25,26]

More recently, with the discovery of 2D van der Waals (vdW) magnets, a comprehensive study has been performed on the spin transport on 2D magnets in planar junctions.[27–32] However, these investigations are restricted to TMR-based devices, i.e., collinear magnetic configurations. There are currently neither experimental nor theoretical works on quantum transport through magnetic skyrmions in 2D vdW magnet planar junctions. Moreover, the Tersoff-Hamann model,[33] which allows explaining the NCMR in STM geometry,[16,19] is questionable if one aims to explore planar tunnel junction devices, where the detecting electrodes are not sharp tips and there is no vacuum gap as in STM experiments.

Here, we demonstrate based on first-principles calculations that the NCMR and the TAMR can be very large in 2D vdW magnets, suggesting the possibility of all-electrical detection of magnetic skyrmions. We study both the regime of tunneling across a vacuum gap as applicable to STM as well as tunnel junction devices with non-magnetic electrodes. We predict a giant NCMR for atomic-scale skyrmions in a graphite/Fe_3GeTe_2/germanene/graphite tunnel junction. The NCMR results from spin mixing of spin-up and -down states of p_z and d_{z^2} character at the surface atoms. Due to orbital symmetry matching at the interface it is enhanced by orders of magnitude in the tunnel device with respect to that obtained in STM geometry. We find a similar enhancement of the TAMR. These magnetoresistance values are at least one order of magnitude larger than those reported so far for conventional transition-metal interfaces.[16,19] Our work also shows the importance of employing non-equilibrium Green's functions (NEGF) for quantum transport of non-collinear spin states in tunnel junctions, where the TH approximation proves inadequate.

Fig. 1 shows a sketch of our proposal for all-electrical skyrmion detection, consisting of Fe_3GeTe_2/germanene (FGT/Ge), a representative 2D vdW heterostructure, sandwiched between two nonmagnetic electrodes, namely tunnel junctions with nonmagnetic electrodes (TJ-NM). A key difference between a TJ-NM and the widely used MTJ setup is that we do not rely on an external magnetic field for device operations. We demonstrate that this setup allows detection of the difference in perpendicular current flow for isolated skyrmions and their ferromagnetic surrounding, enabling an all-electrical detection scheme.

We consider FGT/Ge (Fig. 2a) as a representative 2D vdW magnet heterostructure and skyrmion platform for several reasons. First, there is strong experimental evidence for magnetic skyrmions in vdW FGT heterostructures.[34–37] Second, FGT has a very high Curie temperature, which can vary from 150 K to 220 K depending on Fe occupancy.[38,39] Third, recent theoretical work based on first-principles calculations and atomistic spin simulations predicts that magnetic interactions in FGT/Ge are highly tunable by strain,[40] leading to stabilize nanoscale skyrmions with diameters down to a few nanometers.[41] Finally, the properties of atomically thin vdW layers can be controlled by external stimuli, which makes them ideal skyrmion platforms from a materials design perspective.

Electronic structure and quantum transport calculations were carried out using QUANTUMATK,[42] which uses the non-equilibrium Green function (NEGF)[43] formalism combined with non-collinear density functional theory (DFT).[44] Additionally, we used FLEUR[45] to perform spin spiral calculations based on the generalized Bloch theorem.[46] Computational details are given in Section I in Supporting Information.

NCMR in STM geometry. We start our discussion with the NCMR effect in STM geometry (Fig. 2a) using the TH approach.[33] Due to the large computational cost, we used the smallest Néel-type skyrmion, which fits into a (3×3) FGT/Ge supercell (Fig. 2b). The angle between adjacent spins is 60° and the estimated skyrmion diameter is around 1.2 nm. This is an atomic-scale skyrmion for which quantum transport calculations based on the NEGF formalism are feasible. Note, that only slightly larger skyrmions were found to be stable in atomistic spin simulations using parameters

from DFT.[41] According to the TH model,[33] the differential conductance, dI/dU, in an STM experiment is given by

$$dI/dU(\mathbf{R}_{\mathrm{T}}, U) \propto n(\mathbf{R}_{\mathrm{T}}, E_{\mathrm{F}} + eU) \qquad (1)$$

where $\mathbf{R}_{\mathrm{T}}$ is the tip position, U is the bias voltage, and $n(\mathbf{r}, E)$ is the local density of states (LDOS) of the sample evaluated in the vacuum a few Å above the surface. Even if the STM tip is non-magnetic, the LDOS and thereby the obtained dI/dU signal can be sensitive to the local spin texture due to NCMR,[16] defined for a skyrmion (Sk) in the ferromagnetic (FM) background as NCMR $= \frac{dI/dU_{\mathrm{Sk}} - dI/dU_{\mathrm{FM}}}{dI/dU_{\mathrm{FM}}}$.

The NCMR signal varies locally above the Néel-type skyrmion (Fig. 2b) and reaches a maximum value of about 392 % at the skyrmion core. In a ring around the core the value drops to about -21 % and rises again to about 90 % as one moves further from the center. As expected, the NCMR contrast becomes smaller as one approaches the edge of the skyrmion since the effective noncollinearity is reduced close to the FM environment.

From the energy-resolved vacuum LDOS of the skyrmion core vs. the FM environment (Fig. 2c) evaluated at the skyrmion core above the Te atom, we observe the large NCMR effect of varying positive and negative sign at various energies around E_{F} (Fig. 2d). A similar energy dependence of the NCMR is found at other STM tip positions, and we find that the SOC contribution to the NCMR is rather small. We have also performed calculations for a skyrmion in a (4×4) FGT/Ge supercell with angles of 45° between adjacent spins and a skyrmion diameter of around 1.6 nm, which exhibits an NCMR effect of a similar order of magnitude and lateral variation (see Fig. S2 and Fig. S3 in Supporting Information). Additionally, we have checked the effect of the size of the FM background on NCMR for the same skyrmion size (see Fig. S4 in Supporting Information); the magnitude and energy dependence of the NCMR do not vary significantly if we increase the FM background area.

To go beyond the nanoscale skyrmion (Fig. 2b) and to vary the period of the noncollinear spin structure on a larger scale, we locally approximate the electronic structure in a skyrmion by that of a homogeneous spin spiral state.[46] This approach can explain the experimentally observed NCMR effect of skyrmions and domain walls in ultrathin films.[16,19] Note, that spin-polarized STM was used to resolve domain walls in FGT.[47,48]

Fig. 2e shows the vacuum LDOS calculated about 3 Å above FGT/Ge for spin spirals of different periods. As the spin spiral rotating angle θ varies, one observes significant changes in the height and position of the peaks in the vacuum LDOS (Fig. 2e). We find a prominent peak at about 0.25 eV above E_{F}, which quickly decreases with rising non-collinearity, and one at about 0.75 eV above E_{F}, which shows a more complex change. In contrast, the peak at about 0.5 eV below E_{F} displays only a small shift and broadening.

The corresponding NCMR (Fig. 2f) calculated for various spin spiral states [1] shows a large negative value around $E_{\mathrm{F}} + 0.25$ eV up to about 80 % due to the vanishing peak (cf. Fig. 2e). At larger energies, we find two peaks in the NCMR of up to about 100% and 300%. Note that the spin spiral periods, given by $\lambda = 2\pi/|\mathbf{q}|$, are about 6.5, 3.9, 2.6, 1.9, 1.6 and 1.2 nm for angles of θ = 11°, 18°, 27°, 36°, 45° and 60°, respectively. The NCMR spectrum of the spin spiral state with the shortest period, i.e. largest angle $\theta = 60^\circ$ (red curve in Fig. 2f), is similar in sign and order of magnitude to that obtained for the skyrmion (Fig. 2d) since the rotating angle between neighboring spins in our atomic-scale skyrmion (Fig. 2b) is close to 60°. An exception is the large NCMR peak at about 0.3 eV below E_{F} for skyrmions, which is missing for spin spirals.

The origin of the NCMR for skyrmions can be understood by analyzing the electronic structure. We find the vacuum LDOS (Fig. 3) to be dominated by the p_z and d_{z^2} states of Te2 and Fe3 since these orbitals exhibit the slowest decay into the vacuum. The characteristic changes of the vacuum LDOS for the skyrmion vs. FM state (Fig. 2c), i.e. the shifted double peak structure above E_{F} and the extra peak at about $E_{\mathrm{F}} - 0.3$ eV for the skyrmion, are clearly visible in the Fe3-p_z LDOS

[1] The NCMR spectrum for spin spirals (SS) is calculated by NCMR $= \frac{dI/dU_{\mathrm{SS}} - dI/dU_{\mathrm{FM}}}{dI/dU_{\mathrm{FM}}}$

(Fig. 3a) and in the Te2-p_z and Te2-d_{z^2} LDOS (Fig. 3e,f).

For the spin spiral states, we obtain similar conclusions. The variation of the angle θ between adjacent spins leads to a gradual change of the peaks, e.g., the decreasing peak height in the vacuum LDOS at about $E_{\mathrm{F}} + 0.25$ eV (Fig. 2e). This effect also shows in the Fe3-p_z LDOS (Fig. 3c) and in the Te2-p_z and Te2-d_{z^2} LDOS (Fig. 3g,h). In the LDOS of Fe3-d_{z^2} (Fig. 3d) we notice a shift and decrease of the peak at $E_{\mathrm{F}} - 0.5$ eV which explains the change of the vacuum LDOS at this energy (Fig. 2e). For more detailed p_z- and d_{z^2}-orbital resolved NCMR from the Fe3 and Te2 atoms, see Fig. S5 and Fig. S6 in Supporting Information. Note, that the variations of the orbital decomposed LDOS at the Fe3 and Te2 atoms is also similar for the skyrmion and spin spiral state with the largest angle, i.e. $\theta = 60^\circ$ (red).

The physical mechanism of NCMR can be elucidated through the spin mixing effect, mainly driven by interlayer hopping between Fe3-$d_{z^2}^{\uparrow}$ and Fe2-$p_z^{\downarrow}$, as well as intralayer hopping between Te2-$p_z^{\uparrow}$ and Te2-$p_z^{\downarrow}$. The shift of the $d_{z^2}^{\uparrow}$ peak at about 0.5 eV below E_{F} at the Fe3 atom can be attributed to spin mixing with $p_z^{\downarrow}$ state peak at $E_{\mathrm{F}} - 0.25$ eV of the Fe2 atom (Fig. 4a-b). The spin mixing leads to a shift and splitting of the peaks in both LDOS, and this effect is reproduced and understood by a two-level tight binding (TB) model proposed in Ref.,[19] as shown in Fig. 4c-d. For the p_z states at the Te2 atom a similar effect is found for the states above E_{F} (see Fig. S7 in Supporting Information). Note, that these changes are directly reflected in the vacuum LDOS (Fig. 2e) and can explain the NCMR spectrum above E_{F} (Fig. 2f). See Figs. S8-S10 in Supporting Information for more detailed LDOS of the Te2, Fe3, and Fe2 atoms.

NCMR in tunnel junctions. To properly address NCMR in tunnel junctions, including self-energy due to electrodes and working conditions, one has to calculate the nonequilibrium charge/spin density using the NEGF formalism,[43] going beyond the TH approximation. The transmission function is calculated by NEGF as

$$T(E) = \mathrm{Tr}\left[\mathbf{\Gamma}_{\mathrm{L}}\mathbf{G}\mathbf{\Gamma}_{\mathrm{R}}\mathbf{G}^{\dagger}\right] \qquad (2)$$

where $\mathbf{G}$ is the retarded Green's function of the central region, and $\mathbf{\Gamma}_{\mathrm{L}}/\mathbf{\Gamma}_{\mathrm{R}}$ are matrices describing its coupling to left/right semi-infinite electrodes.

We propose to consider a TJ-NM created by the graphite/FGT/Ge/graphite junction to detect a skyrmion by all-electrical means (Fig. 5a-b). Note, that we used a FGT/Ge (1×1) lattice strained by -3 % as a fixed layer, and a $\sqrt{3} \times \sqrt{3}$ in-plane unit cell of graphite is matched to it. Fig. 5c shows zero-bias transmission functions through an atomic-scale skyrmion (spin structure as in Fig. 2b) and the FM state for the tunnel junction. The junction exhibits an insulating feature for the FM state with a clear dip at E_{F} due to the orbital symmetry matching effect between C-p_z and Te-p_z orbitals at the interface. Note that the hybridization effect between FGT/Ge and the graphite electrodes is small due to the weak vdW interaction (see Fig. S11 in Supporting Information).

The transmission for the skyrmion state (Fig. 5b) exhibits much larger values in a broad energy range, leading to an extremely large NCMR of more than $10,000$ % near E_{F} (Fig. 5c). This value is at least two orders of magnitude higher than that observed for transition-metal interfaces.[16,17,19,49] The NCMR calculated by NEGF differs significantly from that obtained in the TH model (Fig. 5c), especially around E_{F}. The NCMR obtained via the TH approach changes sign several times in the considered energy range and reaches a maximum of about 400% at 0.3 eV below E_{F}. In contrast, the NCMR calculated by NEGF is positive in almost the entire energy range and between $1,000$ and $10,000$ % in a wide range around E_{F}, reaching a maximum value of about $100,000$ %. This demonstrates that the proposed TJ-NM is an ideal platform for all-electrical detection of skyrmions.

The extremely large NCMR observed in TJ-NM stems from the interplay of the symmetry of electronic states and the spin mixing effect. Due to orbital symmetry matching at the interface of FGT/Ge and the graphite electrodes, C-p_z mainly couples to p_z orbitals of the surface atoms of FGT/Ge (Te2, Fe3, and Ge2) (see Fig. S12 and S13 in Supporting Information). The shape of the LDOS at the C atoms in combination with the low p_z LDOS at the Te2, Fe3, and Ge2 atoms near E_{F} can explain the v-shaped transmission functions (see Fig. S14 in Supporting Information). Due to

spin mixing in the skyrmion state the p_z LDOS rises around E_{F} at the Te2 and Fe3 atoms as discussed above – an effect that is also clearly visible in the device setup. This explains the enhanced transmission for the skyrmion state in the vicinity of E_{F}. At energies above $E_{\mathrm{F}} + 0.2$ eV, the NCMR remains positive (Fig. 5c), while the p_z LDOS of the Te2 and Fe3 surface atoms is higher in the FM state between 0.2 and 0.5 eV above E_{F}. Accordingly, the NCMR within the TH model is negative since the tunneling current only depends on the vacuum LDOS that is dominated by surface localized states and not on the coupling of the states to the bulk states. In contrast, for a large transmission obtained by NEGF, the contributing states need to extend through the entire FGT/Ge layer. The higher transmission in the skyrmion and positive NCMR above $E_{\mathrm{F}} + 0.2$ eV indicate that the p_z states, which leads to a large LDOS between $E_{\mathrm{F}} + 0.2$ eV and $E_{\mathrm{F}} + 0.5$ eV in the FM state, contribute little to the current due to their strong localization at the surface atoms. This interpretation is supported by the spatial localization visible in the LDOS map of FGT/Ge (see Fig. S15 in Supporting Information). Note, that a full understanding of the transmission function based only on the LDOS is not feasible. Nevertheless, our analysis illustrates that for a device setup, both interfaces to the electrodes need to be considered and can lead to large enhancements of the NCMR.

We have also calculated the TAMR of our tunnel junction (Fig. S16 in Supporting Information). The obtained value of about 200% near E_{F} is much smaller than the NCMR since the TAMR originates from SOC. However, the value is still more than one order of magnitude larger than the TAMR reported in ultrathin films [12,14,17,18,49] and similar to that reported for molecular junctions, [50–53] showing again the high promise of the proposed TJ-NM for all-electrical skyrmion detection.

Note that due to an extremely high computational cost, we are restricted to an atomic-scale skyrmion in our quantum transport calculations for the device setup. The obtained NCMR (Fig. 5c) applies to a state of densely packed skyrmions or a tunnel junction with a cross-section of the size of the (3×3) 2D unit cell. An increase in the cross-section will lead to a reduction of the NCMR values given here. Skyrmions with a larger diameter, which can be realized experimentally, will also reduce the NCMR as shown by our spin spiral calculations for the STM setup (cf. Fig. 2(e,f)).

However, the key message of our quantum transport calculations is that the NCMR signal is greatly enhanced in a tunnel device with respect to STM geometry (Fig. 5c) due to orbital symmetry matching – an electronic effect due to hybridization at the interface which is expected as well for nanoscale skyrmions. This expectation is supported by the calculation of the TAMR (Fig. S16 in Supporting Information), which is also enhanced by up to one order of magnitude in planar tunnel junctions compared to that in STM geometry due to orbital symmetry matching.

To conclude, we suggest planar devices built from 2D vdW heterostructures such as the graphite/FGT/Ge/graphite tunnel junction considered as an example in our work as ideal platforms for reliable all-electrical skyrmion detection down to the atomically thin limit. Very large NCMR and TAMR are observed in our calculations near the Fermi energy, more than one order of magnitude higher than those reported for transition-metal interfaces. The physical mechanism of the NCMR is explained by the interplay between the spin mixing and orbital symmetry matching effects at the interface. Our work highlights the crucial importance of using the NEGF approach for quantum transport on noncollinear spin structures in tunnel junctions, going beyond the TH model. Our proposal opens a new route to realize skyrmion racetrack memories based on atomically thin vdW materials with full-electrical writing and reading.

Acknowledgement: This study has been supported through the ANR Grant No. ANR-22-CE24-0019. This study has been (partially) supported through the grant NanoX no. ANR-17-EURE-0009 in the framework of the "Programme des Investissements d'Avenir". Financial support from the Deutsche Forschungsgemeinschaft (DFG, German Research Foundation) through SPP2137 "Skyrmionics" (project no. 462602351) is gratefully acknowledged. We acknowledge CALMIP (Grant 2023-[P21008]) and the North-German Supercomputing Alliance (HLRN) for providing HPC resources. We thank M. A. Goerzen and H. Schrautzer for helpful discussions.

Author contributions: D.L. and S. Heinze con-

ceived the project. D.L. and S. Haldar performed spin spiral calculations in 2D van der Waals heterostructures. D.L. performed first-principles quantum transport simulations through individual skyrmions in tunnel junctions. All authors participated in discussions, analyzed the results, and agreed on the contents included. D.L. and S. Haldar prepared the figures. D.L. and S Heinze wrote the manuscript with the input of all authors.

Supporting Information Available

The Supporting Information is available free of charge at `https://pubs.acs.org/`. Computational details, STM tip position and SOC effects on NCMR, the influence of skyrmion size on NCMR in FGT/Ge, the effect of the FM area size on NCMR, orbital-resolved NCMR by the Fe3 and Te2 surface atoms, the spin-mixing effect induced by the Te2 atom, spin- and orbital-resolved LDOS for the Fe3, Fe2 and Te2 atoms, the orbital hybridization effect at the interface between FGT/Ge and graphite electrodes, atom and orbital-resolved LDOS of the FGT/Ge interface for the FM and Sk states, LDOS map, as well as the TAMR calculated by TH in STM geometry and by NEGF in the tunnel junction.

References

(1) Bogdanov, A.; Yablonskii, D. Thermodynamically stable vortices in magnetically ordered crystals. The mixed state of magnets. *Zh. Eksp. Teor. Fiz* **1989**, *95*, 178.

(2) Nagaosa, N.; Tokura, Y. Topological properties and dynamics of magnetic skyrmions. *Nat. Nanotech.* **2013**, *8*, 899–911.

(3) Fert, A.; Reyren, N.; Cros, V. Magnetic skyrmions: advances in physics and potential applications. *Nat. Rev. Mater.* **2017**, *2*, 1–15.

(4) Everschor-Sitte, K.; Masell, J.; Reeve, R.; Kläui, M. Perspective: Magnetic skyrmions Overview of recent progress in an active research field. *J. Appl. Phys.* **2018**, *124*, 240901.

(5) Fert, A.; Cros, V.; Sampaio, J. Skyrmions on the track. *Nat. Nanotechnol.* **2013**, *8*, 152–156.

(6) Luo, S.; Song, M.; Li, X.; Zhang, Y.; Hong, J.; Yang, X.; Zou, X.; Xu, N.; You, L. Reconfigurable Skyrmion Logic Gates. *Nano Lett.* **2018**, *18*, 1180–1184.

(7) Back, C.; Cros, V.; Ebert, H.; Everschor-Sitte, K.; Fert, A.; Garst, M.; Ma, T.; Mankovsky, S.; Monchesky, T. L.; Mostovoy, M.; others The 2020 skyrmionics roadmap. *J. Phys. D: Appl. Phys.* **2020**, *53*, 363001.

(8) Li, S.; Kang, W.; Zhang, X.; Nie, T.; Zhou, Y.; Wang, K.; Zhao, W. Magnetic skyrmions for unconventional computing. *Mater. Horiz.* **2021**, *8*, 854–868.

(9) Psaroudaki, C.; Panagopoulos, C. Skyrmion Qubits: A New Class of Quantum Logic Elements Based on Nanoscale Magnetization. *Phys. Rev. Lett.* **2021**, *127*, 067201.

(10) Heinze, S.; Von Bergmann, K.; Menzel, M.; Brede, J.; Kubetzka, A.; Wiesendanger, R.; Bihlmayer, G.; Blügel, S. Spontaneous atomic-scale magnetic skyrmion lattice in two dimensions. *Nat. Phys.* **2011**, *7*, 713–718.

(11) Romming, N.; Hanneken, C.; Menzel, M.; Bickel, J.; Wolter, B.; von Bergmann, K.; Kubetzka, A.; Wiesendanger, R. Writing and deleting single magnetic skyrmions. *Science* **2013**, *341*, 636–639.

(12) Bode, M.; Heinze, S.; Kubetzka, A.; Pietzsch, O.; Nie, X.; Bihlmayer, G.; Blügel, S.; Wiesendanger, R. Magnetization-Direction-Dependent Local Electronic Structure Probed by Scanning Tunneling Spectroscopy. *Phys. Rev. Lett.* **2002**, *89*, 237205.

(13) Gould, C.; Rüster, C.; Jungwirth, T.; Girgis, E.; Schott, G. M.; Giraud, R.; Brunner, K.; Schmidt, G.; Molenkamp, L. W. Tunneling Anisotropic Magnetoresistance: A

Spin-Valve-Like Tunnel Magnetoresistance Using a Single Magnetic Layer. *Phys. Rev. Lett.* **2004**, *93*, 117203.

(14) von Bergmann, K.; Menzel, M.; Serrate, D.; Yoshida, Y.; Schröder, S.; Ferriani, P.; Kubetzka, A.; Wiesendanger, R.; Heinze, S. Tunneling anisotropic magnetoresistance on the atomic scale. *Phys. Rev. B* **2012**, *86*, 134422.

(15) Hervé, M.; Dupé, B.; Lopes, R.; Böttcher, M.; Martins, M. D.; Balashov, T.; Gerhard, L.; Sinova, J.; Wulfhekel, W. Stabilizing spin spirals and isolated skyrmions at low magnetic field exploiting vanishing magnetic anisotropy. *Nat. Commun.* **2018**, *9*, 1015.

(16) Hanneken, C.; Otte, F.; Kubetzka, A.; Dupé, B.; Romming, N.; Von Bergmann, K.; Wiesendanger, R.; Heinze, S. Electrical detection of magnetic skyrmions by tunnelling non-collinear magnetoresistance. *Nat. Nanotechnol.* **2015**, *10*, 1039–1042.

(17) Crum, D. M.; Bouhassoune, M.; Bouaziz, J.; Schweflinghaus, B.; Blügel, S.; Lounis, S. Perpendicular reading of single confined magnetic skyrmions. *Nat. Commun.* **2015**, *6*, 8541.

(18) Kubetzka, A.; Hanneken, C.; Wiesendanger, R.; von Bergmann, K. Impact of the skyrmion spin texture on magnetoresistance. *Phys. Rev. B* **2017**, *95*, 104433.

(19) Perini, M.; Meyer, S.; Kubetzka, A.; Wiesendanger, R.; Heinze, S.; von Bergmann, K. Electrical Detection of Domain Walls and Skyrmions in Co Films Using Noncollinear Magnetoresistance. *Phys. Rev. Lett.* **2019**, *123*, 237205.

(20) Muckel, F.; von Malottki, S.; Holl, C.; Pestka, B.; Pratzer, M.; Bessarab, P.; Heinze, S.; Morgenstern, M. Experimental identification of two distinct skyrmion collapse mechanisms. *Nat. Phys.* **2021**, *17*, 395–402.

(21) Franz, C.; Freimuth, F.; Bauer, A.; Ritz, R.; Schnarr, C.; Duvinage, C.; Adams, T.; Blügel, S.; Rosch, A.; Mokrousov, Y.; Pfleiderer, C. Real-Space and Reciprocal-Space Berry Phases in the Hall Effect of $Mn_{1x}Fe_xSi$. *Phys. Rev. Lett.* **2014**, *112*, 186601.

(22) Kanazawa, N.; Kubota, M.; Tsukazaki, A.; Kozuka, Y.; Takahashi, K. S.; Kawasaki, M.; Ichikawa, M.; Kagawa, F.; Tokura, Y. Discretized topological Hall effect emerging from skyrmions in constricted geometry. *Phys. Rev. B* **2015**, *91*, 041122.

(23) Maccariello, D.; Legrand, W.; Reyren, N.; Garcia, K.; Bouzehouane, K.; Collin, S.; Cros, V.; Fert, A. Electrical detection of single magnetic skyrmions in metallic multilayers at room temperature. *Nat. Nanotechnol.* **2018**, *13*, 233–237.

(24) He, B.; Tomasello, R.; Luo, X.; Zhang, R.; Nie, Z.; Carpentieri, M.; Han, X.; Finocchio, G.; Yu, G. All-Electrical 9-Bit Skyrmion-Based Racetrack Memory Designed with Laser Irradiation. *Nano Lett.* **2023**, *23*, 9482–9490.

(25) Penthorn, N. E.; Hao, X.; Wang, Z.; Huai, Y.; Jiang, H. W. Experimental Observation of Single Skyrmion Signatures in a Magnetic Tunnel Junction. *Phys. Rev. Lett.* **2019**, *122*, 257201.

(26) Chen, S. et al. All-Electrical Skyrmionic Bits in a Chiral Magnetic Tunnel Junction. **2023**, 2302.08020, arXiv, https://doi.org/10.48550/arXiv.2302.08020 (accesed February 2, 2024).

(27) Song, T.; Cai, X.; Tu, M. W.-Y.; Zhang, X.; Huang, B.; Wilson, N. P.; Seyler, K. L.; Zhu, L.; Taniguchi, T.; Watanabe, K.; others Giant tunneling magnetoresistance in spin-filter van der Waals heterostructures. *Science* **2018**, *360*, 1214–1218.

(28) Klein, D. R.; MacNeill, D.; Lado, J. L.; Soriano, D.; Navarro-Moratalla, E.; Watanabe, K.; Taniguchi, T.; Manni, S.; Canfield, P.; Fernández-Rossier, J.; others Probing magnetism in 2D van der Waals crys-

talline insulators via electron tunneling. *Science* **2018**, *360*, 1218–1222.

(29) Paudel, T. R.; Tsymbal, E. Y. Spin Filtering in CrI_3 Tunnel Junctions. *ACS Appl. Mater. Interfaces* **2019**, *11*, 15781–15787.

(30) Wang, Z.; Sapkota, D.; Taniguchi, T.; Watanabe, K.; Mandrus, D.; Morpurgo, A. F. Tunneling spin valves based on Fe_3GeTe_2/hBN/Fe_3GeTe_2 van der Waals heterostructures. *Nano Lett.* **2018**, *18*, 4303–4308.

(31) Li, X.; Lü, J.-T.; Zhang, J.; You, L.; Su, Y.; Tsymbal, E. Y. Spin-Dependent Transport in van der Waals Magnetic Tunnel Junctions with Fe_3GeTe_2 Electrodes. *Nano Lett.* **2019**, *19*, 5133–5139.

(32) Min, K.-H.; Lee, D. H.; Choi, S.-J.; Lee, I.-H.; Seo, J.; Kim, D. W.; Ko, K.-T.; Watanabe, K.; Taniguchi, T.; Ha, D. H.; others Tunable spin injection and detection across a van der Waals interface. *Nat. Mater.* **2022**, *21*, 1144–1149.

(33) Tersoff, J.; Hamann, D. R. Theory of the scanning tunneling microscope. *Phys. Rev. B* **1985**, *31*, 805–813.

(34) Ding, B.; Li, Z.; Xu, G.; Li, H.; Hou, Z.; Liu, E.; Xi, X.; Xu, F.; Yao, Y.; Wang, W. Observation of Magnetic Skyrmion Bubbles in a van der Waals Ferromagnet Fe_3GeTe_2. *Nano Lett.* **2020**, *20*, 868–873.

(35) Wu, Y.; Zhang, S.; Zhang, J.; Wang, W.; Zhu, Y.; Hu, J.; Yin, G.; Wong, K.; Fang, C.; Wan, C.; others Néel-type skyrmion in WTe_2/Fe_3GeTe_2 van der Waals heterostructure. *Nat. Commun.* **2020**, *11*, 3860.

(36) Park, T. et al. Néel-type skyrmions and their current-induced motion in van der Waals ferromagnet-based heterostructures. *Phys. Rev. B* **2021**, *103*, 104410.

(37) Wu, Y.; Francisco, B.; Chen, Z.; Wang, W.; Zhang, Y.; Wan, C.; Han, X.; Chi, H.; Hou, Y.; Lodesani, A.; Yin, G.; Liu, K.; Cui, Y.; Wang, K.; Moodera, J. A Van der Waals Interface Hosting Two Groups of Magnetic Skyrmions. *Adv. Mater.* **2022**, *34*, 2110583.

(38) Deng, Y.; Yu, Y.; Song, Y.; Zhang, J.; Wang, N.; Sun, Z.; Yi, Y.; Wu, Y.; Wu, S.; Zhu, J.; others Gate-tunable room-temperature ferromagnetism in two-dimensional Fe_3GeTe_2. *Nature* **2018**, *563*, 94–99.

(39) Li, Q.; Yang, M.; Gong, C.; Chopdekar, R.; NDiaye, A.; Turner, J.; Chen, G.; Scholl, A.; Shafer, P.; Arenholz, E.; others Patterning-induced ferromagnetism of Fe_3GeTe_2 van der Waals materials beyond room temperature. *Nano Lett.* **2018**, *18*, 5974–5980.

(40) Li, D.; Haldar, S.; Drevelow, T.; Heinze, S. Tuning the magnetic interactions in van der Waals Fe_3GeTe_2 heterostructures: A comparative study of ab initio methods. *Phys. Rev. B* **2023**, *107*, 104428.

(41) Li, D.; Haldar, S.; Heinze, S. Strain-Driven Zero-Field Near-10 nm Skyrmions in Two-Dimensional van der Waals Heterostructures. *Nano Lett.* **2022**, *22*, 7706–7713.

(42) Smidstrup, S. et al. QuantumATK: an integrated platform of electronic and atomic-scale modelling tools. *J. Phys. Condens. Matter* **2019**, *32*, 015901.

(43) Brandbyge, M.; Mozos, J.-L.; Ordejón, P.; Taylor, J.; Stokbro, K. Density-functional method for nonequilibrium electron transport. *Phys. Rev. B* **2002**, *65*, 165401.

(44) Eich, F. G.; Gross, E. K. U. Transverse Spin-Gradient Functional for Noncollinear Spin-Density-Functional Theory. *Phys. Rev. Lett.* **2013**, *111*, 156401.

(45) Welcome to the FLEUR-project. www.flapw.de (accessed Sept. 1, 2022).

(46) Kurz, P.; Förster, F.; Nordström, L.; Bihlmayer, G.; Blügel, S. Ab initio treatment of noncollinear magnets with the full-potential linearized augmented plane wave method. *Phys. Rev. B* **2004**, *69*, 024415.

(47) Yang, H.-H.; Bansal, N.; RüSSmann, P.; Hoffmann, M.; Zhang, L.; Go, D.; Li, Q.; Haghighirad, A.-A.; Sen, K.; Blügel, S.; Tacon, M. L.; Mokrousov, Y.; Wulfhekel, W. Magnetic domain walls of the van der Waals material Fe_3GeTe_2. *2D Materials* **2022**, *9*, 025022.

(48) Trainer, C.; Armitage, O. R.; Lane, H.; Rhodes, L. C.; Chan, E.; Benedičič, I.; Rodriguez-Rivera, J. A.; Fabelo, O.; Stock, C.; Wahl, P. Relating spin-polarized STM imaging and inelastic neutron scattering in the van der Waals ferromagnet $\mathrm{Fe_3GeTe_2}$. *Phys. Rev. B* **2022**, *106*, L081405.

(49) Schäfer-Richarz, J. F.; Risius, P.; Czerner, M.; Heiliger, C. Magnetic tunnel junctions: An efficient way for electrical skyrmion detection investigated by ab initio theory. *Phys. Rev. B* **2019**, *100*, 214413.

(50) Li, J.-J.; Bai, M.-L.; Chen, Z.-B.; Zhou, X.-S.; Shi, Z.; Zhang, M.; Ding, S.-Y.; Hou, S.-M.; Schwarzacher, W.; Nichols, R. J.; others Giant single-molecule anisotropic magnetoresistance at room temperature. *J. Am. Chem. Soc.* **2015**, *137*, 5923–5929.

(51) Rakhmilevitch, D.; Sarkar, S.; Bitton, O.; Kronik, L.; Tal, O. Enhanced Magnetoresistance in Molecular Junctions by Geometrical Optimization of Spin-Selective Orbital Hybridization. *Nano Lett.* **2016**, *16*, 1741–1745.

(52) Li, D.; Pauly, F.; Smogunov, A. Giant anisotropic magnetoresistance through a tilted molecular π-orbital. *Phys. Rev. Res.* **2020**, *2*, 033184.

(53) Otte, F.; Heinze, S.; Mokrousov, Y. Molecular anisotropic magnetoresistance. *Phys. Rev. B* **2015**, *92*, 220411(R).

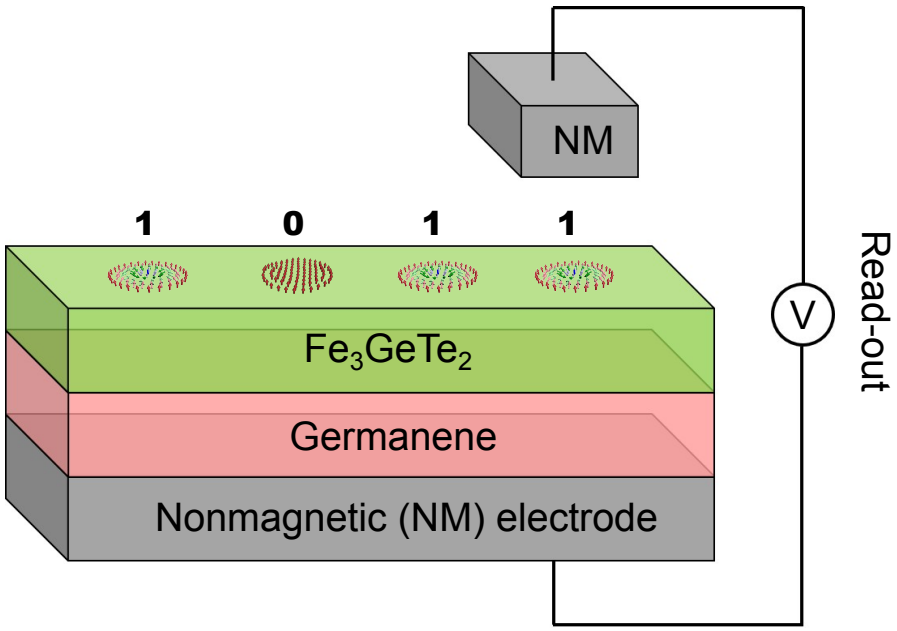

Figure 1: Schematic representation of the proposed vertical tunnel junctions with nonmagnetic electrodes (TJ-NM) for electrical read-out of skyrmions in 2D vdW magnets, e.g., in racetrack memory. The skyrmions are stabilized at the Fe_3GeTe_2/germanene vdW heterostructure. Reading data from the skyrmion pattern is accomplished all electrically based on NCMR.

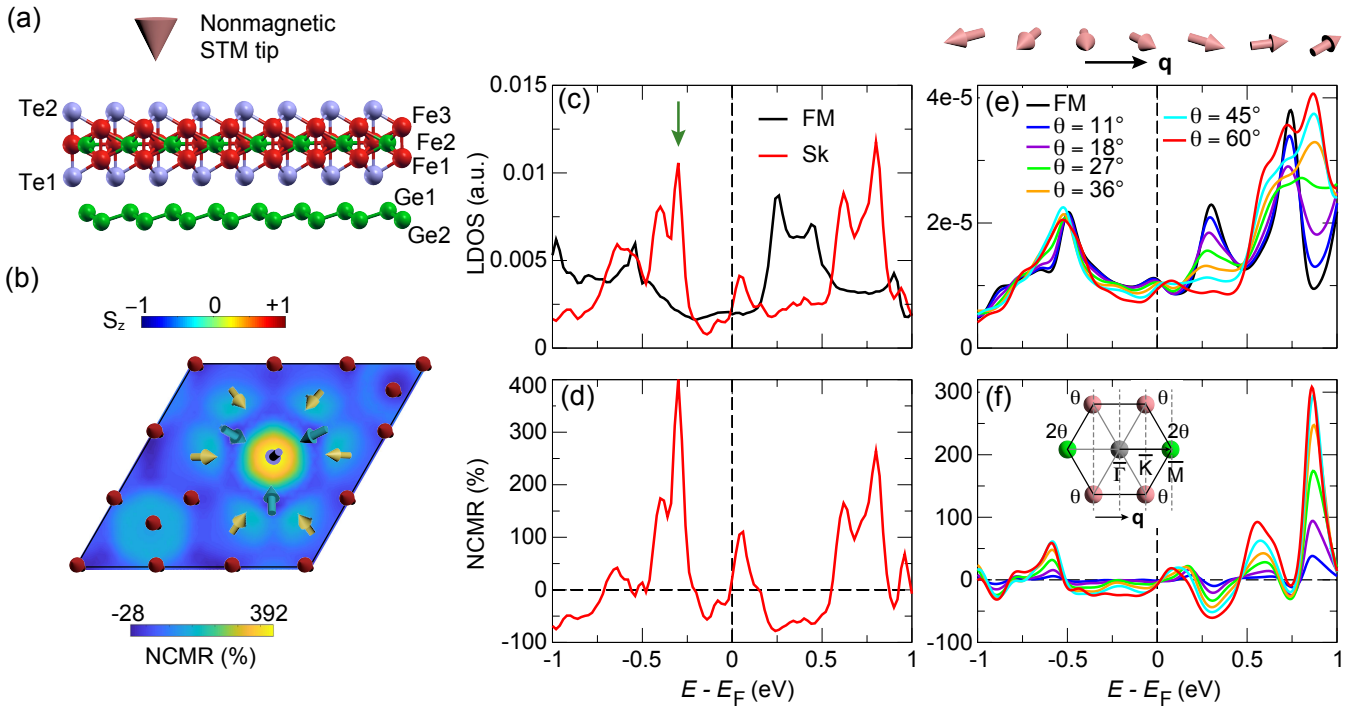

Figure 2: Calculated NCMR in STM geometry using the TH approximation. (a) Schematic plot of an STM experiment on FGT/Ge with a non-magnetic tip. (b) Spin structure of the nanoscale Néel-type skyrmion stabilized in strained FGT/Ge[41] and the NCMR map calculated at a distance of 3 Å from the surface and an energy of $E = E_F - 0.3$ eV. (c) Vacuum LDOS for the FM state (black) and the Sk state (red). The green arrow marks the energy at which the NCMR map in panel (b) has been plotted. (d) NCMR calculated from the LDOS of the FM and Sk states shown in panel (c). (e) LDOS in the vacuum calculated for spin spiral states at 3 Å above FGT/Ge for various nearest-neighbor angles θ. (f) NCMR calculated from the LDOS of the FM and spin spiral states shown in panel (e). The inset shows the hexagonal atomic lattice with the spin spiral vector $\mathbf{q}$ along the $\overline{\Gamma} - \overline{\mathrm{K}} - \overline{\mathrm{M}}$ direction of the 2D Brillouin zone and the angle θ between spins on neighboring sites.

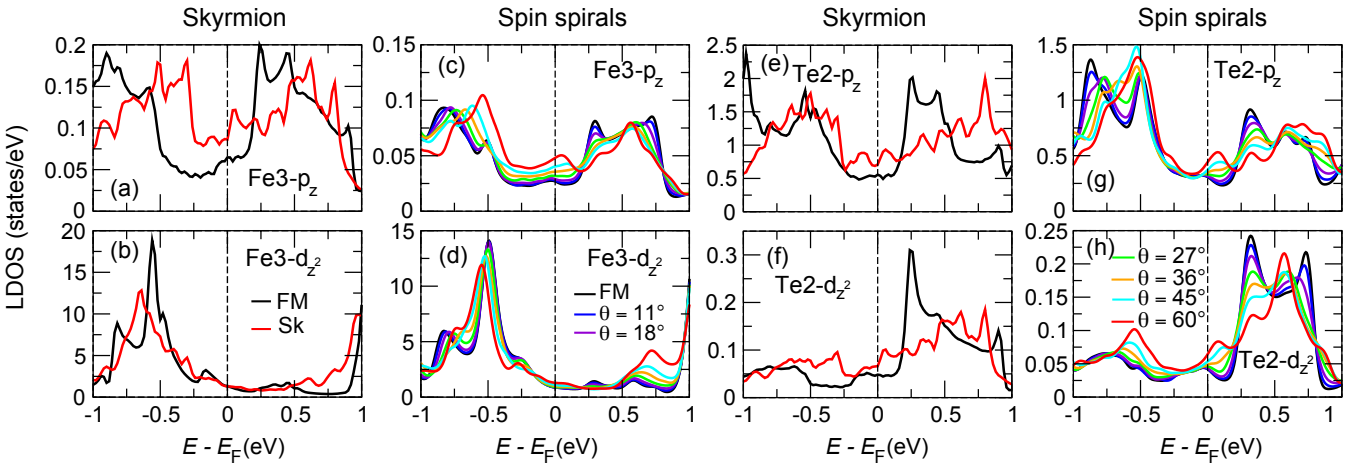

Figure 3: LDOS of (a) p_z and (b) d_{z^2} character in the FM (black) and in the skyrmion state (red) for the Fe3 (surface) atom (cf. Fig. 2a) in the FGT/Ge heterostructure. Note, that the sum of spin-up and -down states is shown. (c-d) as (a-b) for the spin spiral state for various angles θ between adjacent magnetic moments. (e-h) as (a-d) for the Te2 (surface) atom.

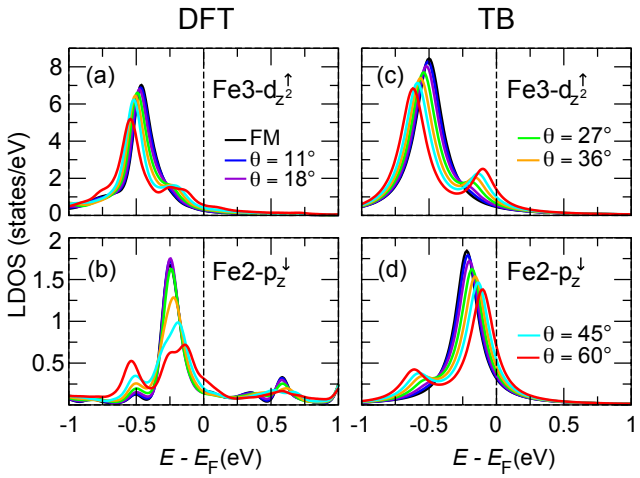

Figure 4: NCMR mechanism by spin-mixing in FGT/Ge. LDOS of Fe3-$d_{z^2}^{\uparrow}$ (a) and Fe2-$p_z^{\downarrow}$ (b) states as obtained from DFT calculations for spin spiral states with an angle θ between adjacent spins. (c-d) The same as in (a-b) but using a two-level TB model proposed in Ref.[19] (See Section I in Supporting Information for more details.)

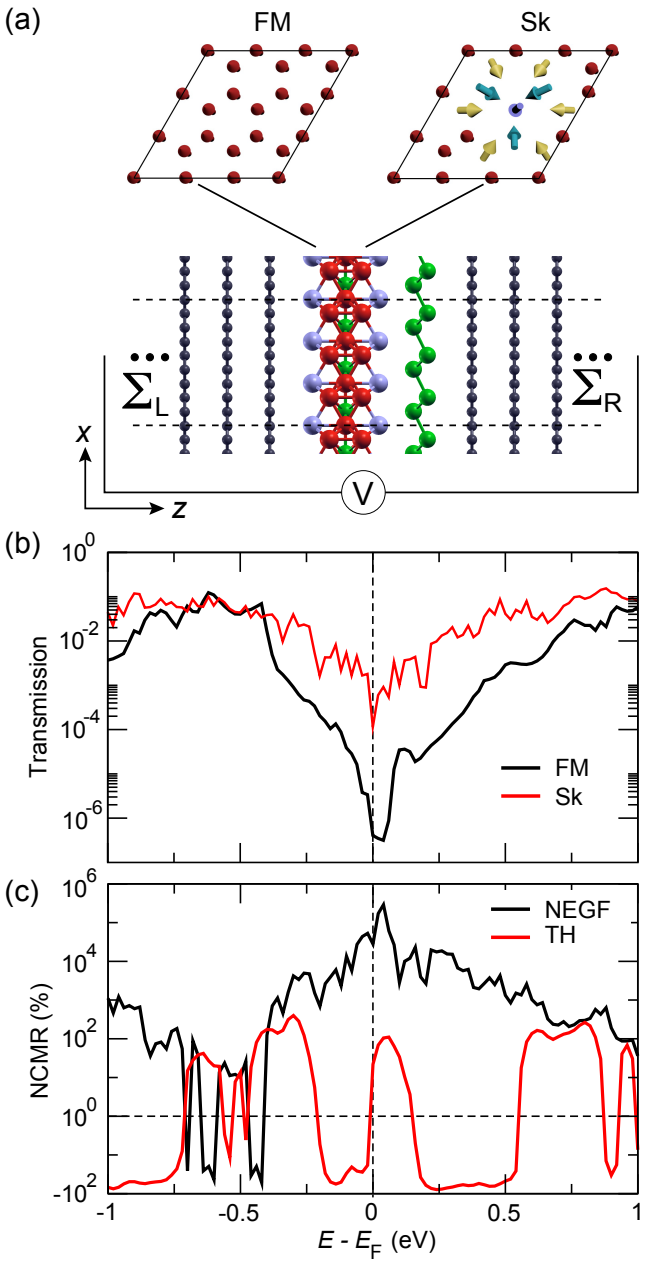

Figure 5: Calculated NCMR in tunnel junctions using the NEGF formalism. (a) Side view of the atomic structure of the graphite/FGT/Ge/graphite junction device used for measuring current difference in the FM and Sk state. (b) Transmission functions for the FM state (black), and the (3×3) Néel-type Sk state (red). (c) The corresponding NCMR (black), defined as NCMR $= [T_{\mathrm{Sk}}(E) - T_{\mathrm{FM}}(E)]/T_{\mathrm{FM}}(E)$, calculated by NEGF. The NCMR obtained in the TH approximation (red) is shown for comparison (same data as in Fig. 2d).

TOC Graphic

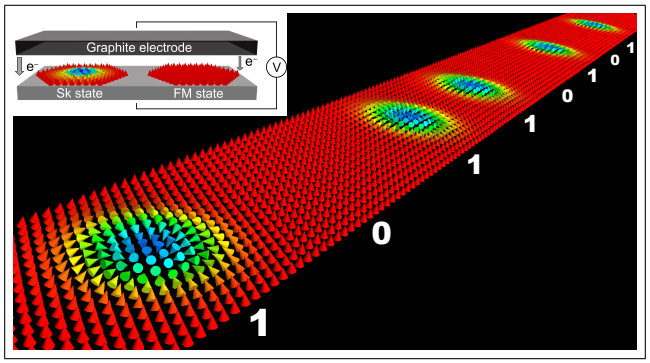

Supporting Information for "Proposal for all-electrical skyrmion detection in van der Waals tunnel junctions"

Dongzhe Li,[1,*] Soumyajyoti Haldar,[2,†] and Stefan Heinze[2,3]

[1] *CEMES, Université de Toulouse, CNRS, 29 rue Jeanne Marvig, F-31055 Toulouse, France*

[2] *Institute of Theoretical Physics and Astrophysics, University of Kiel, Leibnizstrasse 15, 24098 Kiel, Germany*

[3] *Kiel Nano, Surface, and Interface Science (KiNSIS), University of Kiel, 24118 Kiel, Germany*

(Dated: February 14, 2024)

I. Computational methods

Electronic structure calculations. For the atomic structure relaxations of the tunnel junction studied in this work, we took into account vdW interactions using semi-empirical dispersion corrections as formulated by Grimme [1] in order to accurately describe the vdW gap between different 2D materials. To obtain the NCMR within the TH approximation, we calculate homogeneous spin spiral states based on the generalized Bloch theorem using the FLEUR code [2, 3]. The full-potential linearized augmented plane wave (FLAPW) method used in FLEUR ranks amongst the most accurate implementations of DFT. Spin spirals can be characterized by the wave vector $\mathbf{q}$ from the 2D Brillouin zone (BZ), and the magnetic moment of an atom at lattice site $\mathbf{R}_i$ is given by $\mathbf{M}_i = M[\cos(\mathbf{q}\cdot\mathbf{R}_i), \sin(\mathbf{q}\cdot\mathbf{R}_i), 0]$, where M is the magnitude of the magnetic moment. Here, $\mathbf{q}$ represents a vector in reciprocal space, which we choose along the high symmetry direction $\overline{\Gamma} - \overline{\mathrm{K}} - \overline{\mathrm{M}}$ of the 2D BZ. Note, that the $\overline{\Gamma}$ point corresponds to the FM state. To calculate the NCMR, we rotate our spin spiral directions with canting angles between 0° and 60° with respect to the FM state. We used a cutoff parameter for FLAPW basis functions of k_{max} = 4.1 a.u.$^{-1}$, and we included basis functions including spherical harmonics up to l_{max} = 8. We have performed all calculations using local density approximation (LDA). We have used 44×44 and 64×64 $\mathbf{k}$-point meshes to obtain well-converged charge densities for different $\mathbf{q}$ vectors and corresponding vacuum LDOS calculations at 3 Å above the film surface, respectively.

Quantum transport calculations. Noncollinear DFT calculations were performed using the linear combination of atomic orbitals (LCAO) and PZ parametrization of LDA for the exchange functional, as implemented in the QUANTUMATK code [4]. The accuracy of the LCAO basis-set in QUANTUMATK has been carefully checked by comparing it to FLEUR [5] (see also Fig. S1). We used the PseudoDojo (medium) numerical LCAO basis set, which resulted, as we have checked, in good agreement with the FLEUR results [5]. The energy mesh cut for the real-space grid is chosen as 100 Hartree. We have shown recently by first-principles calculations that the efficient control of the magnetic interactions by strain allows stabilizing zero-field nanoscale skyrmions in FGT/Ge [6]. Therefore, we used an FGT/Ge (1×1) lattice strained by -3 % as a fixed layer, and a $\sqrt{3}\times\sqrt{3}$ in-plane unit cell of graphite is matched to it. As we have checked, such a matching of the in-plane lattice, resulting in graphite compressed by 4.3%, leads to no significant change in its band structure. A 3×3 in-plane periodicity (9 atoms per Fe layer) was employed to avoid artificial skyrmion-skyrmion interactions, this corresponds to the smallest skyrmion stabilized in the strained FGT/Ge interface (see the main text), as demonstrated in Ref. 6 by atomistic spin simulations with parameters from DFT. Our transport setup for graphite/FGT/Ge/graphite junction contains a total of 396 atoms.

The noncollinear spin version of the nonequilibrium Greens function (NEGF) formalism was employed to calculate transmission functions, defining the coherent conductance in the framework of the Landauer-Büttiker formalism as shown in Eq. 2 in the main text. The density matrix was converged using 6×6 $\mathbf{k}$ points, while the transmission functions were evaluated using a much denser $\mathbf{k}$-mesh of 32×32. Additionally, vacuum LDOS calculations were performed using a $\mathbf{k}$-mesh of 48×48. These $\mathbf{k}$-meshes are adequate to numerically stabilize the relevant observable.

Tight binding model. To explain the spin mixing effect observed from DFT calculations, we adopted a two-level analytically solvable TB model proposed in Ref. 7. The angle-dependent hopping between two levels ($\uparrow$ and $\downarrow$) is given by $t = t_0 \sin\theta/2$, where θ is the spin spiral rotating angle. The following parameters are used in order to reproduce the DFT results: $\epsilon_\uparrow = -0.50$, $\epsilon_\downarrow = -0.22$, $\gamma_\uparrow = 0.12$, $\gamma_\downarrow = 0.10$, and $t_0 = 0.50$. Here, ϵ and γ denote the on-site level and the degree of hybridization with the neighboring atoms. All parameters are given in eV.

* Corresponding author: dongzhe.li@cemes.fr

† haldar@physik.uni-kiel.de

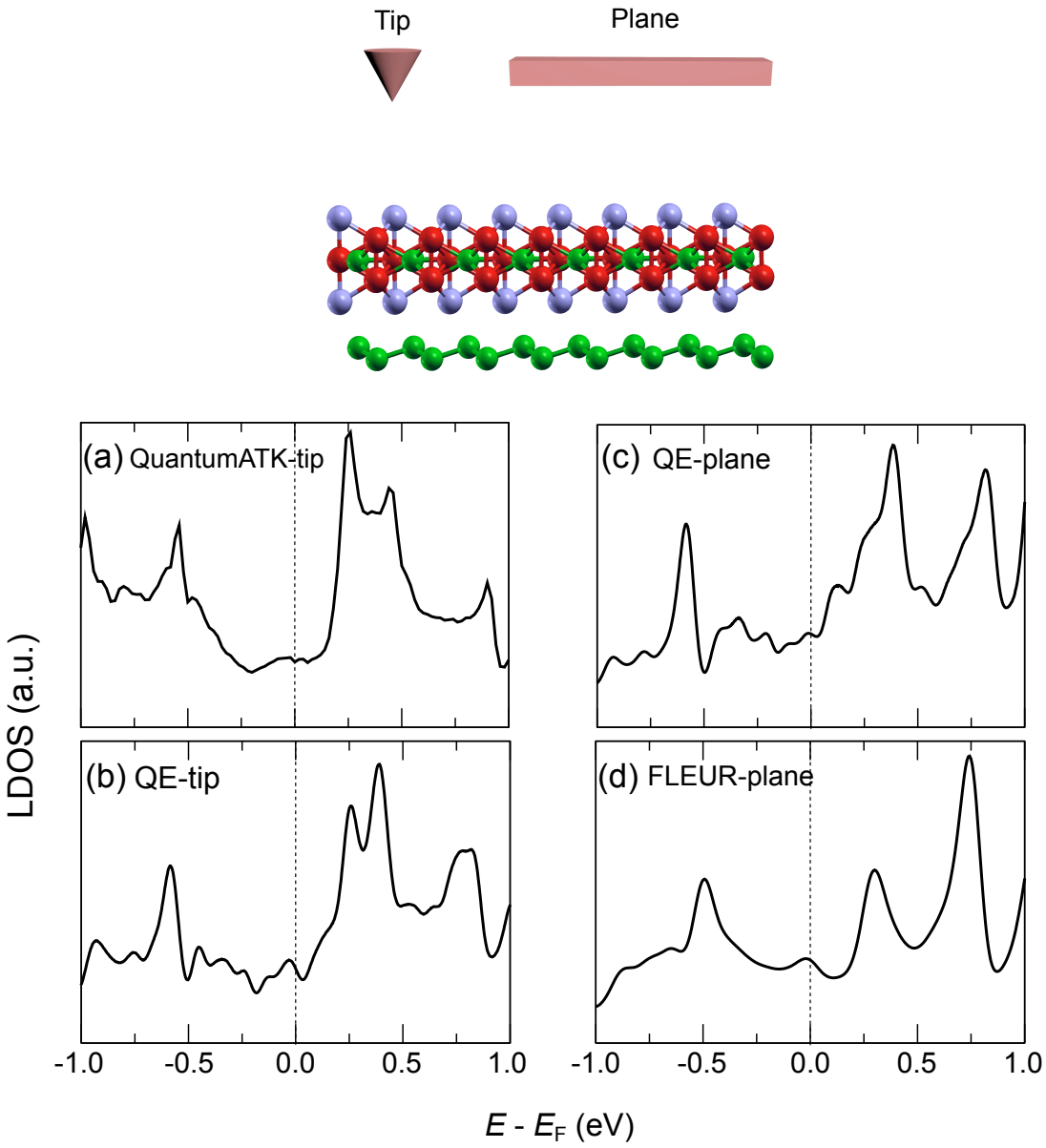

Figure S 1. The LDOS in the vacuum at 3 Å above the FGT/Ge heterostructure calculated by different DFT codes: (a) QUANTUMATK [4] t, (b,c) QUANTUM ESPRESSO (QE) [8], and (d) FLEUR [2] for the ferromagnetic state without SOC. Note, that using QUANTUMATK the vacuum LDOS has been integrated in a small lateral area above the surface, which simulates the effect of an STM tip on top of the surface Te atom (see sketch above). In the calculation using FLEUR the LDOS is integrated in-plane over the entire two-dimensional unit cell of FGT/Ge (see sketch above). In QE both methods have been applied. These show that the differences between the calculations with QUANTUMATK and FLEUR originate in the different lateral integration which has been applied. A good general agreement between different codes is found in terms of energy level alignment.

II. Tunneling anisotropic magnetoresistance

Experimentally, tunneling anisotropic magnetoresistance (TAMR) originates from spin-orbit coupling (SOC) and is mixed with the NCMR signal during all-electrical detection. Quantitatively, TAMR is defined as

$$\mathrm{TAMR} = (G_\perp - G_\parallel)/G_\parallel \tag{1}$$

where $G_\parallel$ and $G_\perp$ are electrical conductances for parallel and perpendicular orientations of the magnetization, respectively, with regard to the current flow.

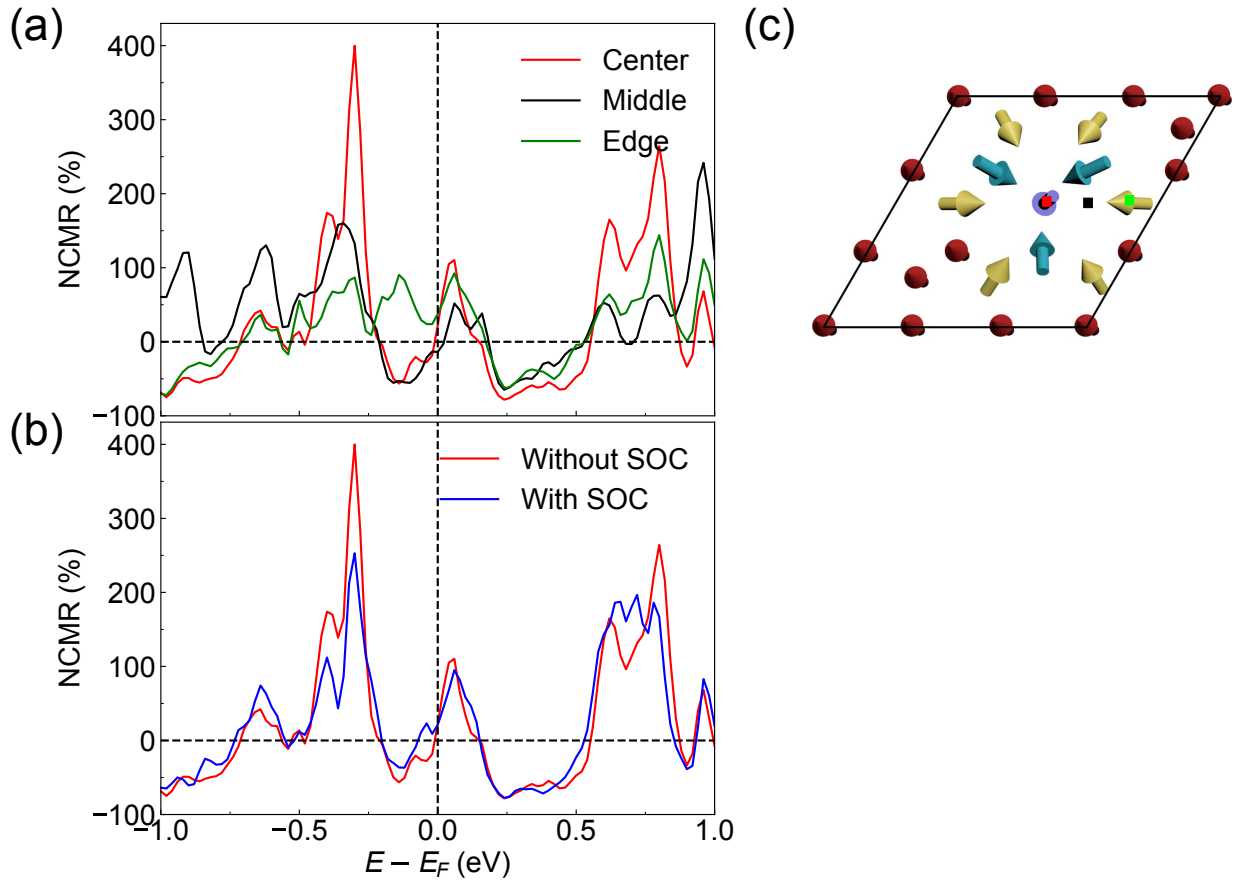

Figure S 2. STM tip position and SOC effects on NCMR. (a) NCMR calculated with STM tips of three different positions for FGT/Ge, namely center, middle, and edge of the skyrmion. (b) NCMR calculated on top of the center of the skyrmion with and without SOC for FGT/Ge. (c) The skyrmion spin structure with different STM box positions is presented, namely red, blue, and green boxes corresponding to the positions of the center, middle, and edge of the skyrmion, respectively.

Fig. S16a shows the atomic structure of a vdW TJ-NM consisting of a single FGT layer sandwiched between two metallic semi-infinite graphite electrodes along the z-axis, i.e., the direction of current flow. An FGT monolayer is a metallic ferromagnet as seen from the sizable electron density at the Fermi energy, E_{F}, and the exchange splitting in the calculated density of states (see e.g. Ref. 5). We find a strong out-of-plane magnetocrystalline anisotropy energy (MAE) of about 0.95 meV/Fe for the FGT monolayer favoring a magnetization direction along the z-axis, i.e. along the junction, which is also reflected by the energy as a function of the magnetization direction (inset of Fig. S16c). This indicates a large SOC effect on tunnel junctions based on FGT. The impact of SOC on electron transport in the graphite/FGT/Ge/graphite junction is shown in Fig. S16b. The transmission function has been calculated for a magnetization direction of FGT being either parallel or perpendicular to the current flow. Surprisingly, although graphite is semi-metal and FGT is metallic, the whole junction behaves like an insulator. The dip-like feature observed for both spin orientation directions at the Fermi energy is due to the p_z orbital characteristics of the graphite electrodes, which couples selectively to Te-p_z and d_{z^2} orbitals via the orbital matching effect. The transmission function depends strongly on the magnetization direction of the FGT layer with respect to the current flow, resulting in a giant TAMR of more than 200% near E_{F}. Such a TAMR value is more than one order of magnitude larger than TAMR values reported in ultrathin films [9–13] and similar to that reported for molecular junctions [14–16]. This indicates that the graphite/FGT/Ge/graphite junction is a promising platform for all-electrical detection of spin textures.

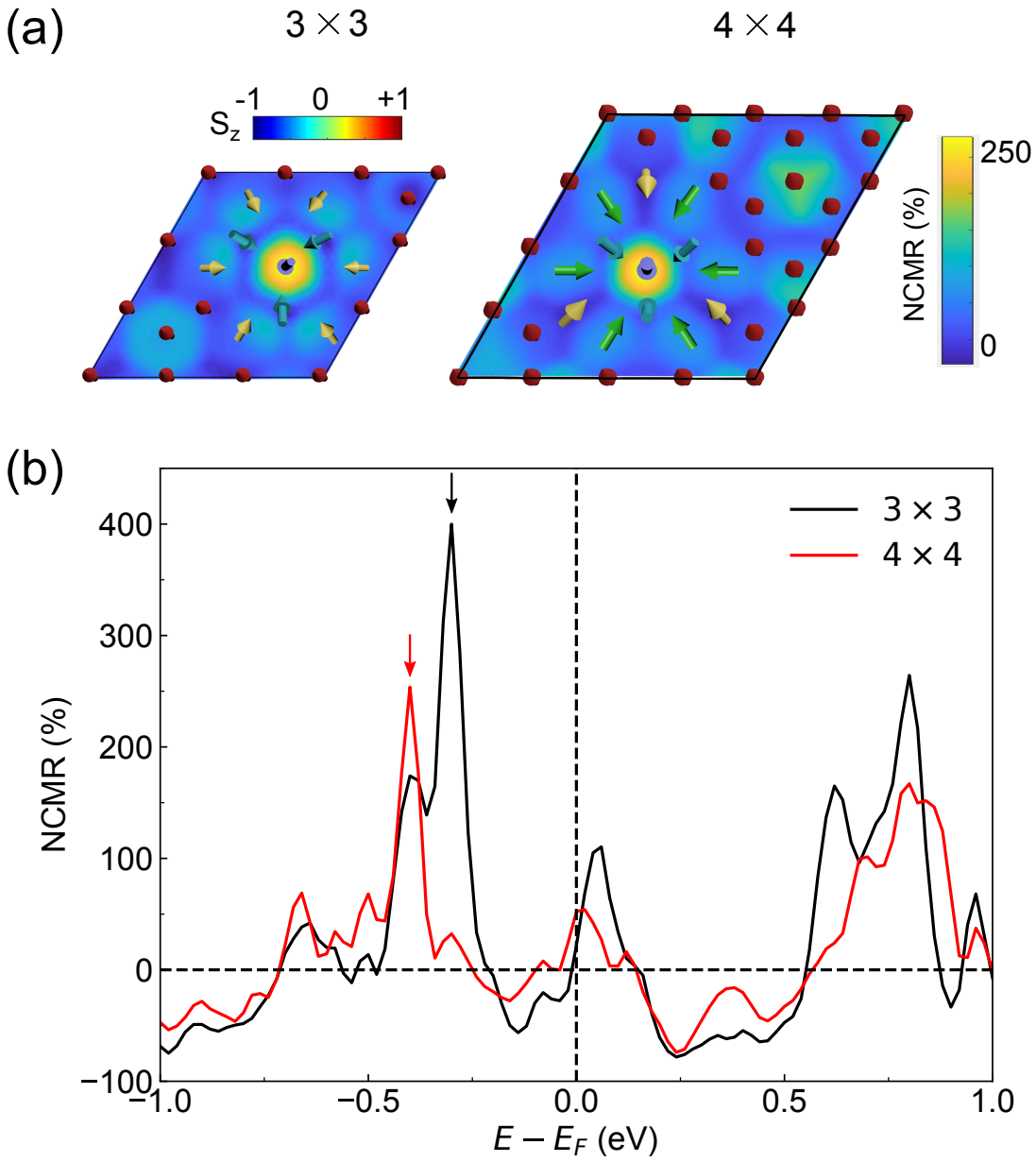

Figure S 3. Influence of Skyrmion Size on NCMR in FGT/Ge. (a) NCMR map calculated at the height of 3 Å above the 3×3 and 4×4 skyrmions for FGT/Ge at energies E_F-0.3 eV and E_F-0.4 eV, respectively. (b) Energy-dependent NCMR spectrum calculated at the center of the skyrmion. The arrows indicate the energy used to plot the NCMR maps presented in (a).

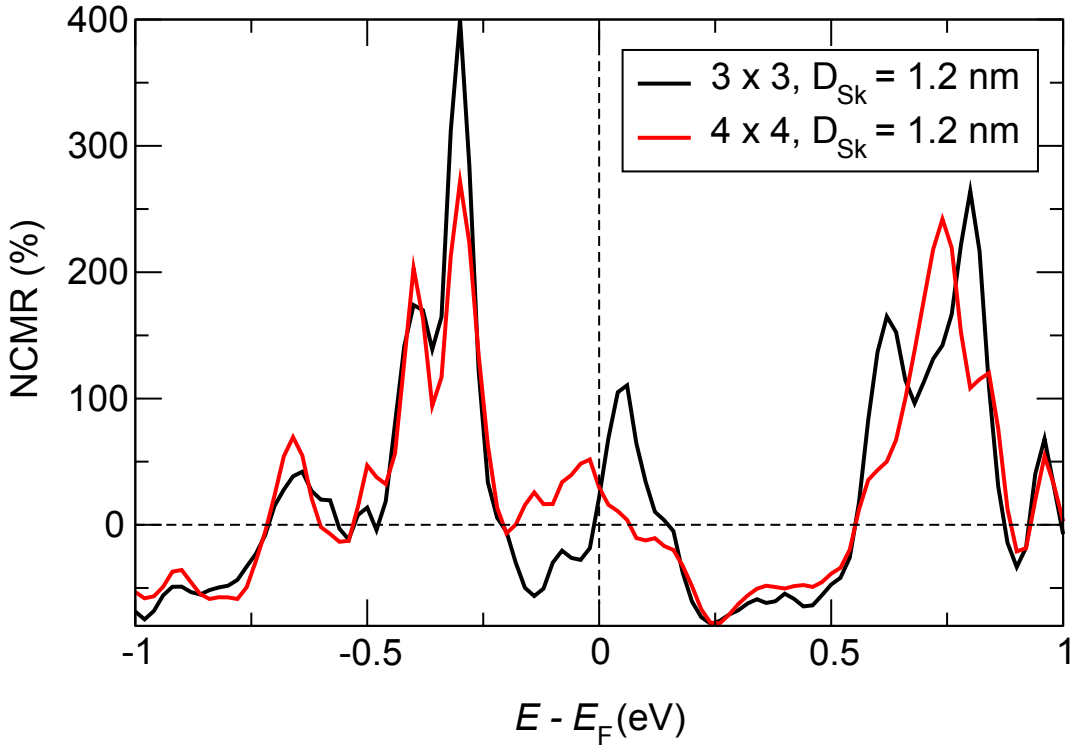

Figure S 4. NCMR for the 1.2 nm size skyrmion calculated within the TH approximation but using different supercell sizes: 3×3 (black) and 4×4 (red) unit cells. The only difference between the two skyrmion setups is that the 4×4 unit cell contains more FM background.

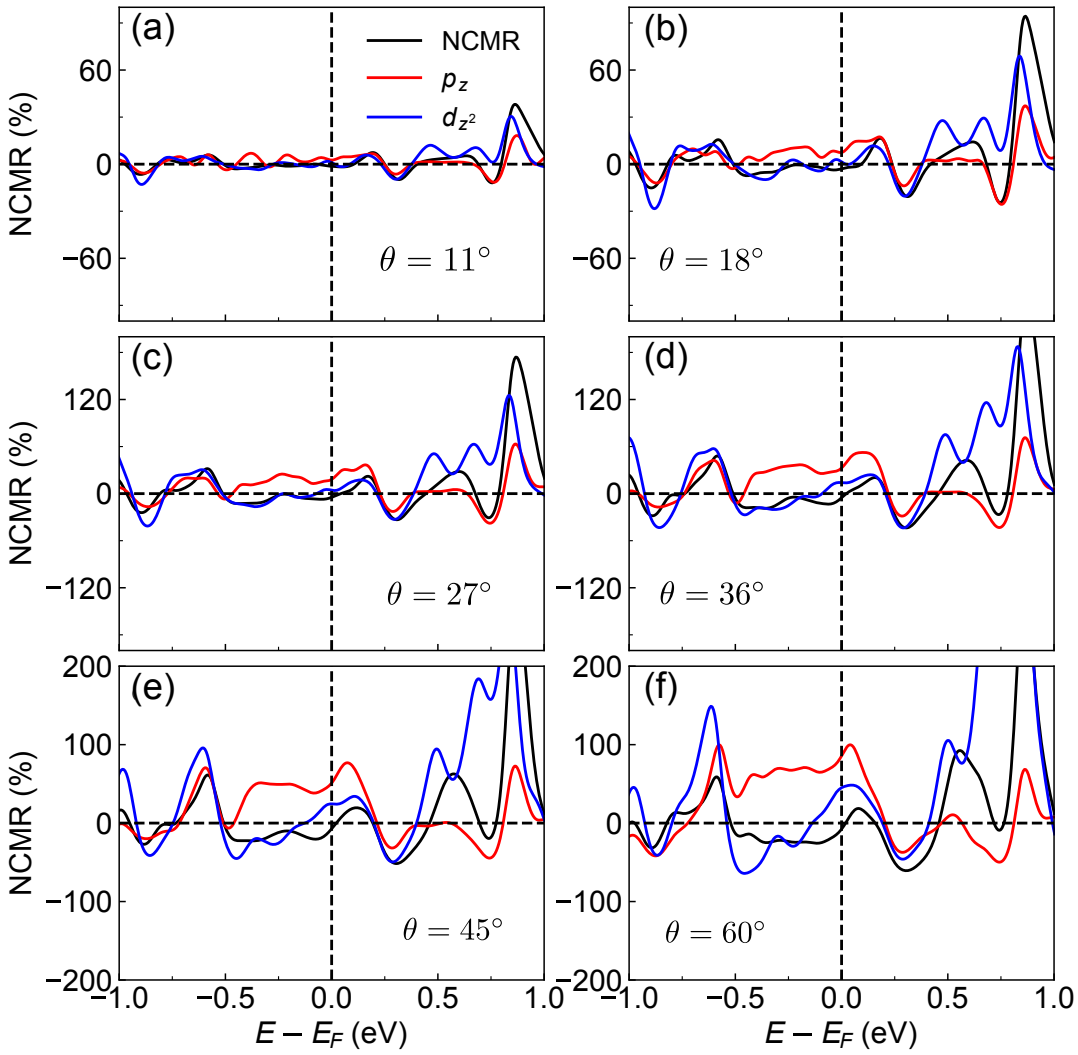

Figure S 5. Orbital-resolved NCMR by the Fe3 (surface) atom. Vacuum NCMR vs. Orbital (p_z and d_{z^2}) decomposed NCMR comparison for $\theta = 11°$ (a), $\theta = 18°$ (b), $\theta = 27°$ (c), $\theta = 36°$ (d), $\theta = 45°$ (e), and $\theta = 60°$ (f).

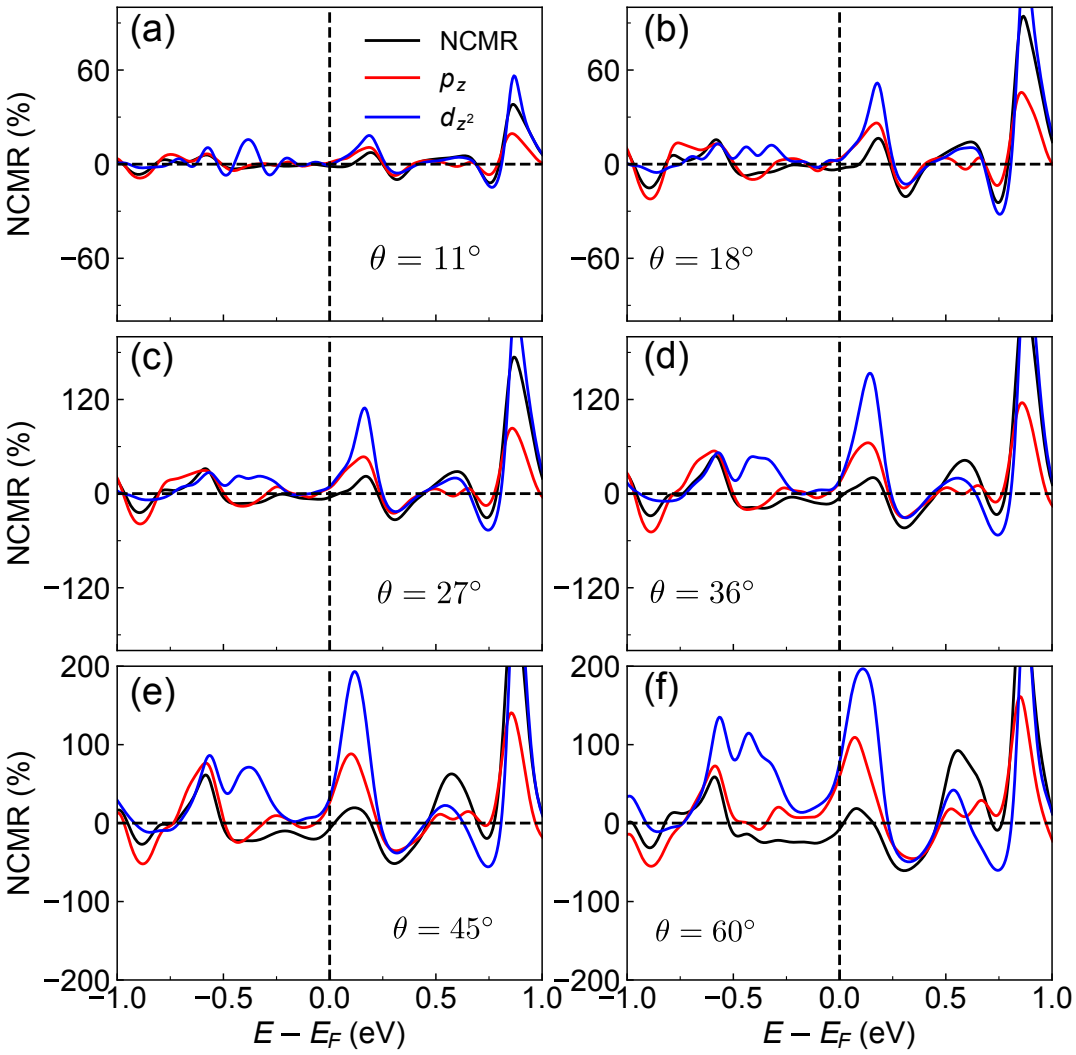

Figure S 6. The same as Supplementary Figure 5 but for the Te2 (surface) atom.

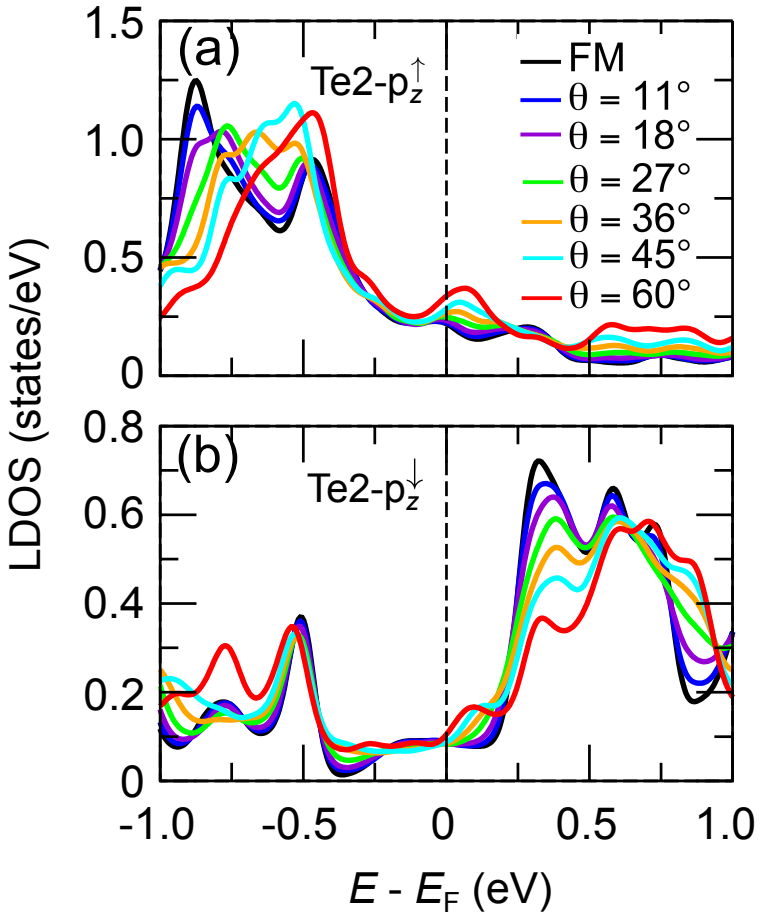

Figure S 7. The Te2 atom induced spin-mixing effect. (a) spin-up states with p_z at the Te surface atom, and (b) spin-down states with p_z at the Te surface atom. The LDOS is shown in every panel for spin spiral states with various angle θ between adjacent spin moments. Here, the peak at about 0.25 eV above $E_{\rm F}$ in the $p_z^{\downarrow}$ states hybridizes with a state at a similar energy in the $p_z^{\uparrow}$ states. This spin mixing leads to the diminishing of the peak at about 0.25 eV, a new peak just above $E_{\rm F}$, and the peak structure in the p_z states at energies above $E_{\rm F} + 0.5$ eV.

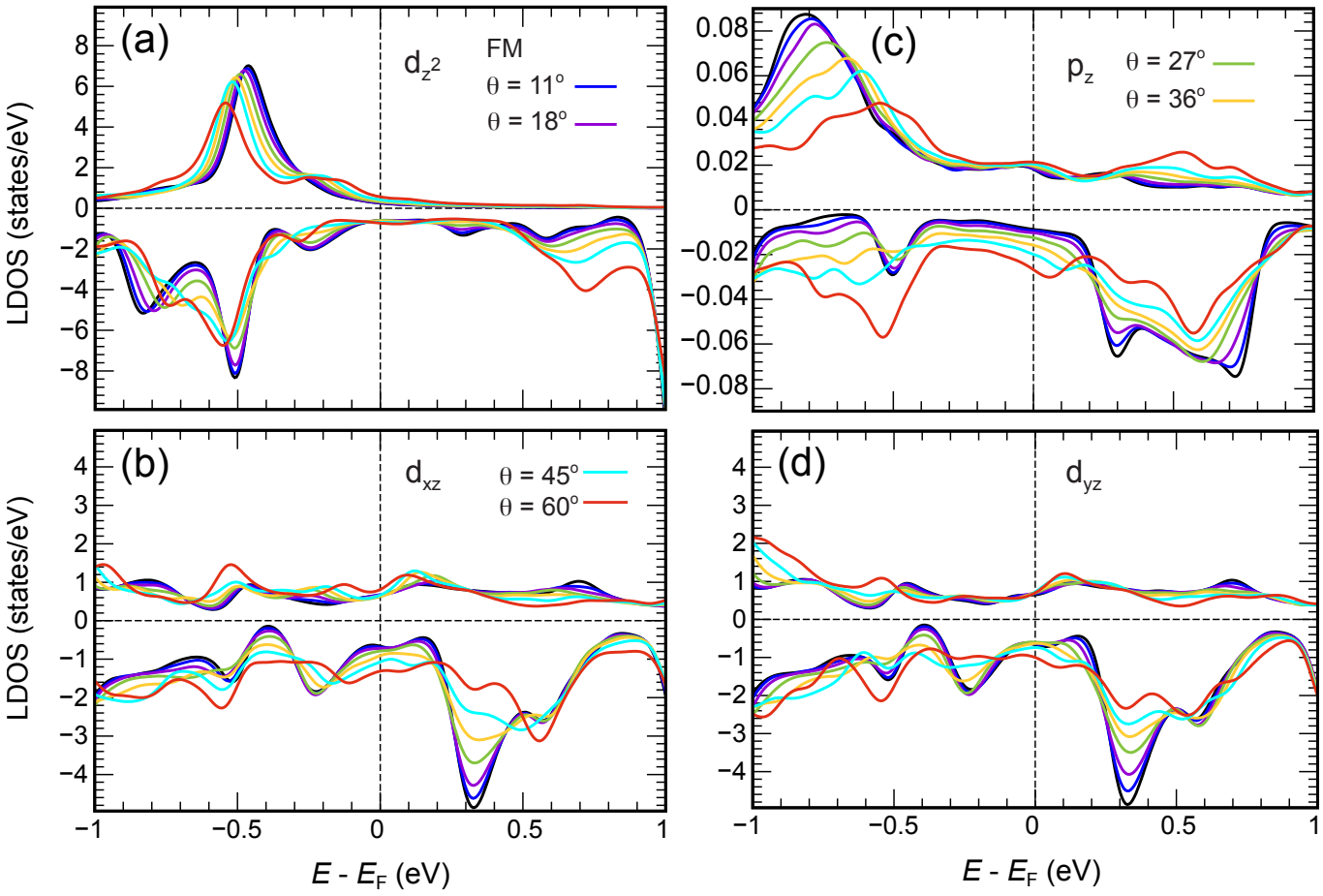

Figure S 8. Spin- and orbital-resolved local density of states. Local density of states (LDOS) of (a) d_{z^2}, (b) p_z, (c) d_{xz} and (d) d_{yz} orbital character on Fe3 atom (surface) of FGT/Ge for homogeneous spin spirals along the direction $\mathbf{q} = (\overline{\Gamma} \rightarrow \overline{\mathrm{K}} \rightarrow \overline{\mathrm{M}})$. The angle between spins on neighboring sites is indicated in the legends. Spin-up and -down LDOS is given in each panel. The LDOS has been calculated using the FLEUR code.

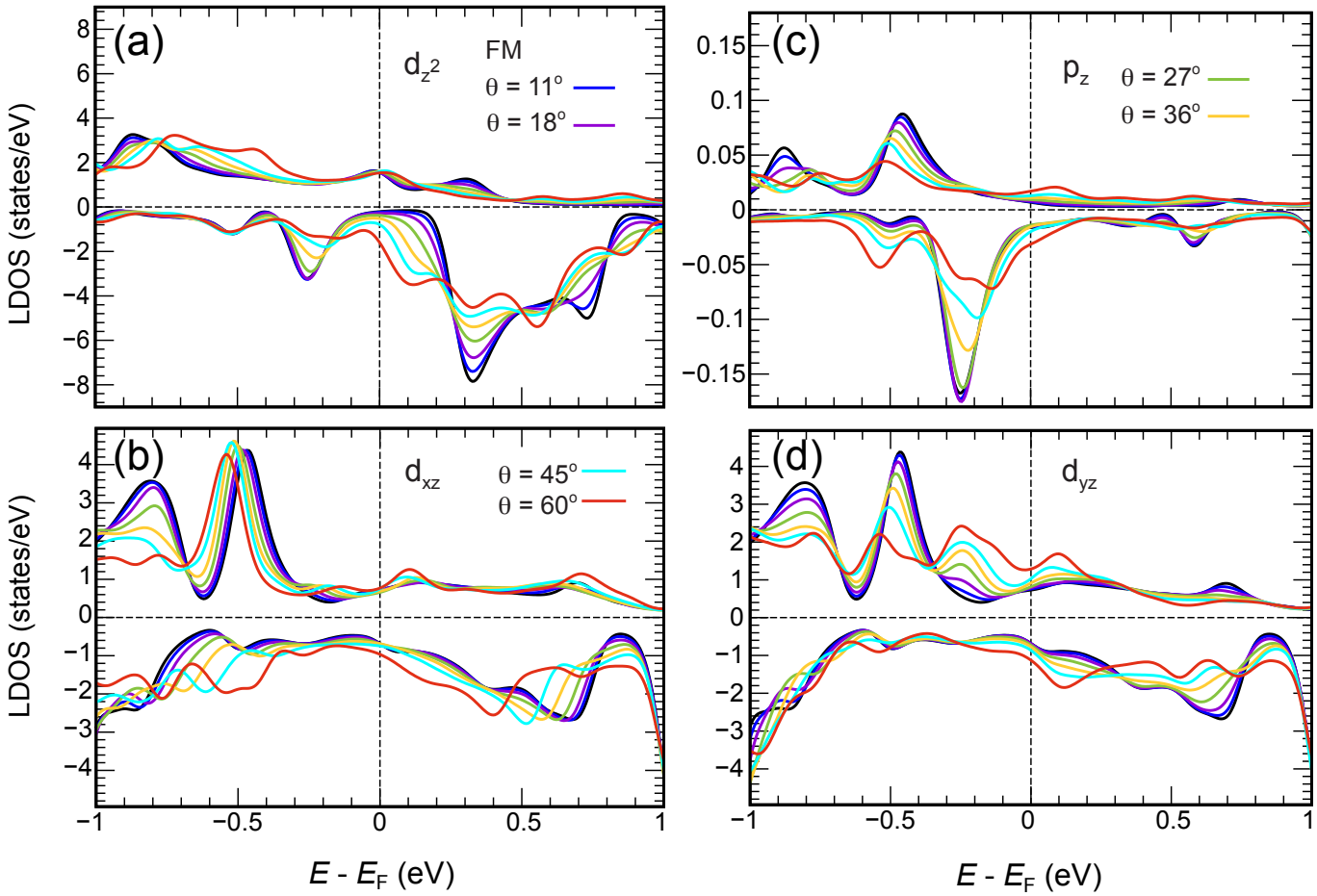

Figure S 9. The same as Supplementary Figure 8 but for the Fe2 atom.

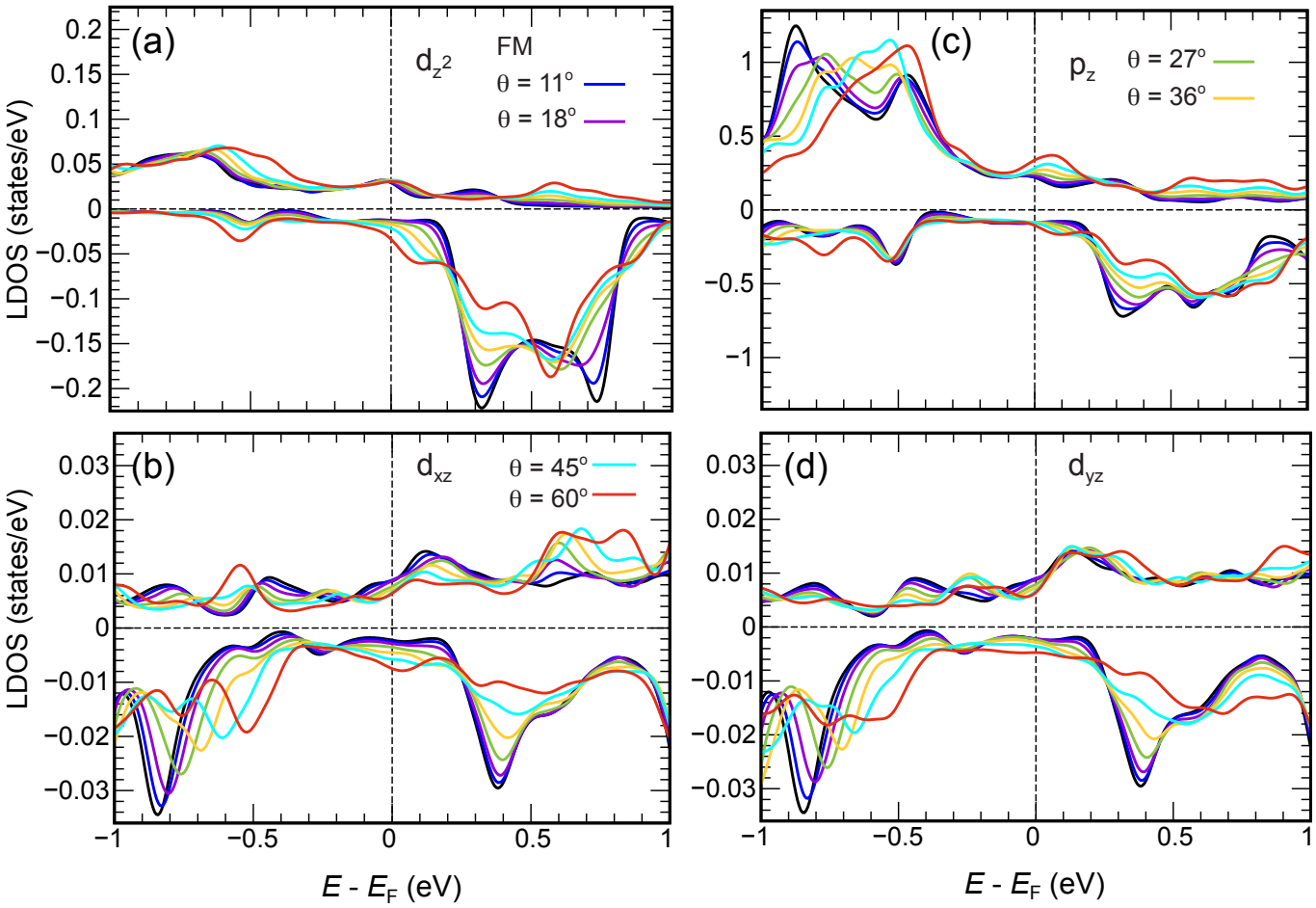

Figure S 10. The same as Supplementary Figure 8 but for the surface Te2 atom.

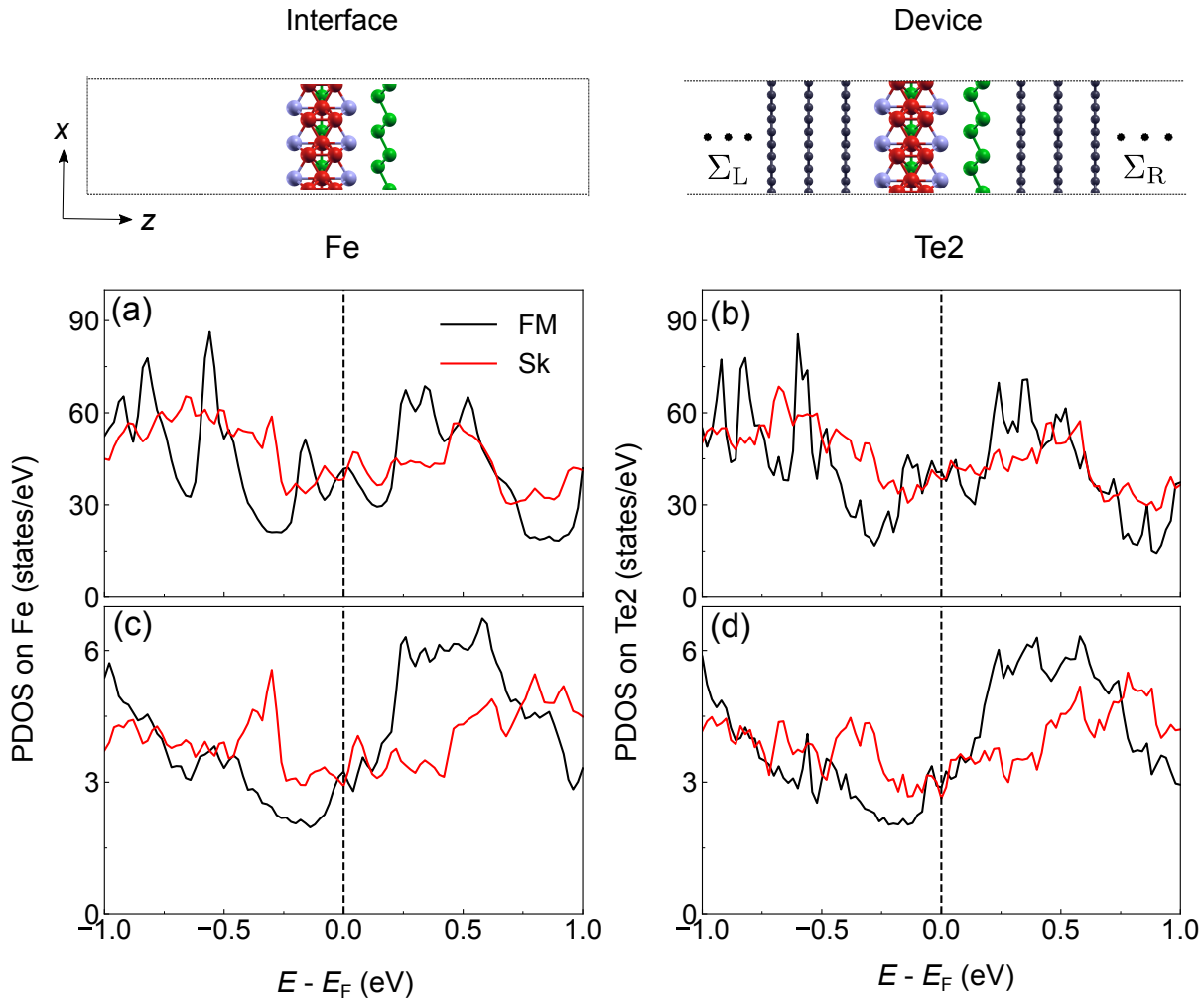

Figure S 11. Orbital hybridization effect at the interface between FGT/Ge and graphite electrodes. (a-b) Projected density of states (PDOS) on Fe (combined contributions from Fe1, Fe2, and Fe3) and Te2 atoms at FGT/Ge (slab model with the periodic boundary condition (PBC) in the z direction). (c-d) The same as (a-b) but for the graphite/FGT/Ge/graphite tunnel junction (semi-infinite left/right electrodes without PBC in the z direction).

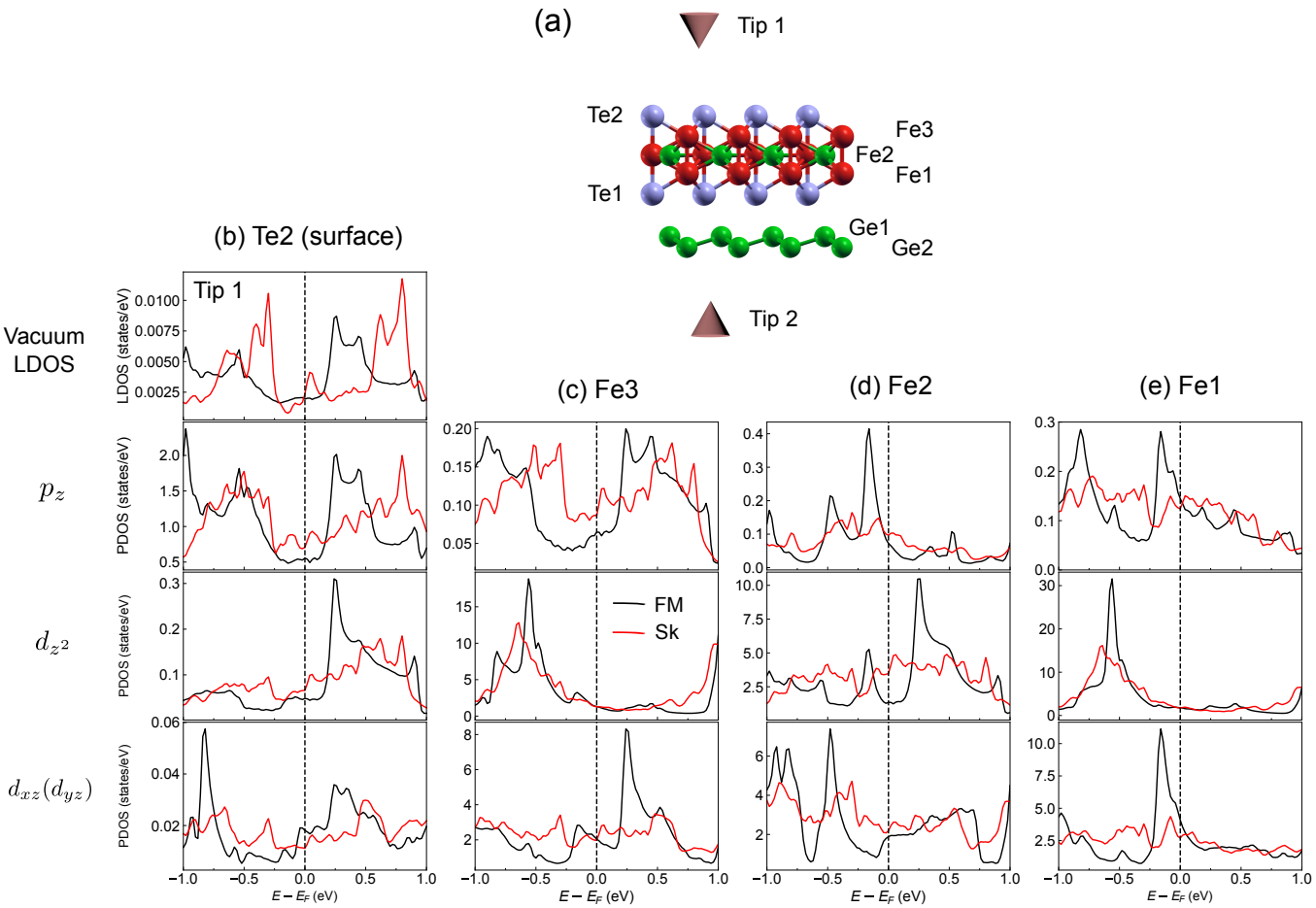

Figure S 12. Atom and orbital-resolved PDOS of the FGT/Ge interface for the FM and Sk states. (a) Atomic structure of FGT/Ge with two STM tip positions, one is 3Åon top of the FGT layer (Tip 1), and another one is on the bottom of the Ge layer (Tip 2). (b) Vacuum LDOS on Tip 1 and PDOS on the Fe3 atom. (c-d) The same as (a) but for Fe2 and Te atoms. (c) Vacuum LDOS on Tip 2 and PDOS on the Ge1 atom. (f) The same as (c) but for the Ge2 atom.

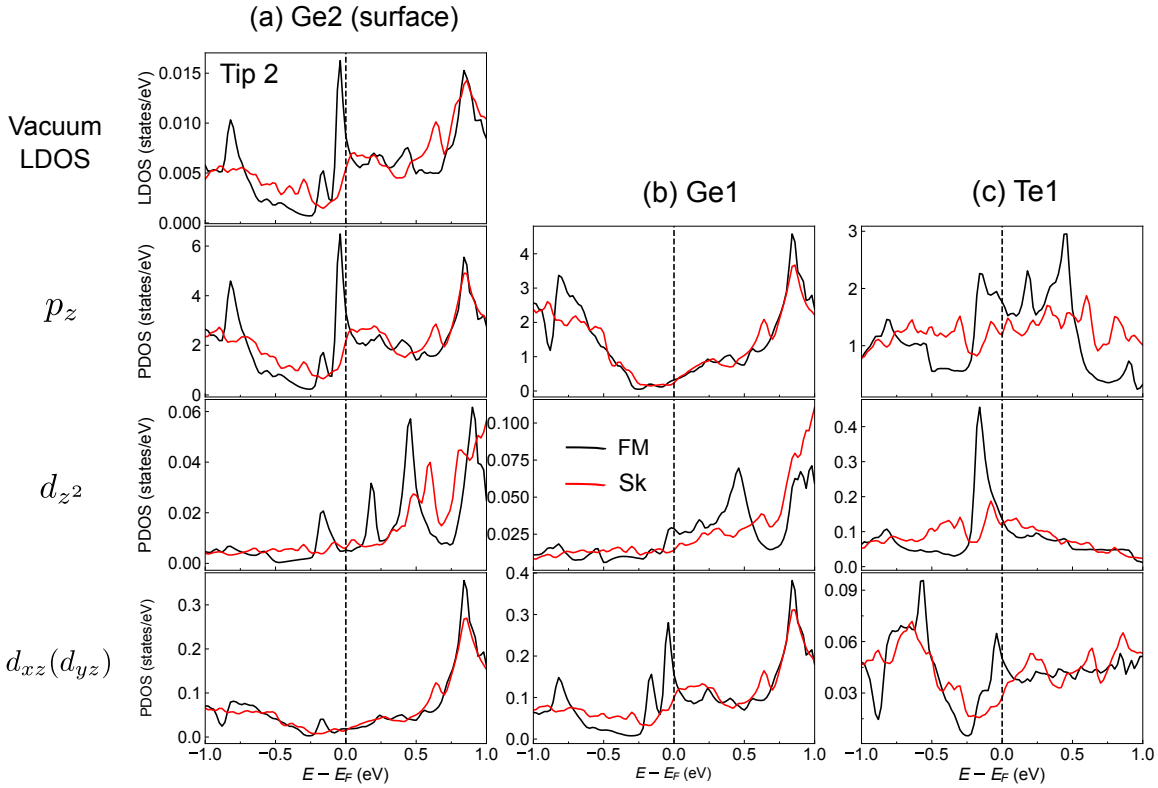

Figure S 13. The same as Supplementary Figure 8 but for the Ge2 (a), Ge1 (b), and Te1 (c) atoms.

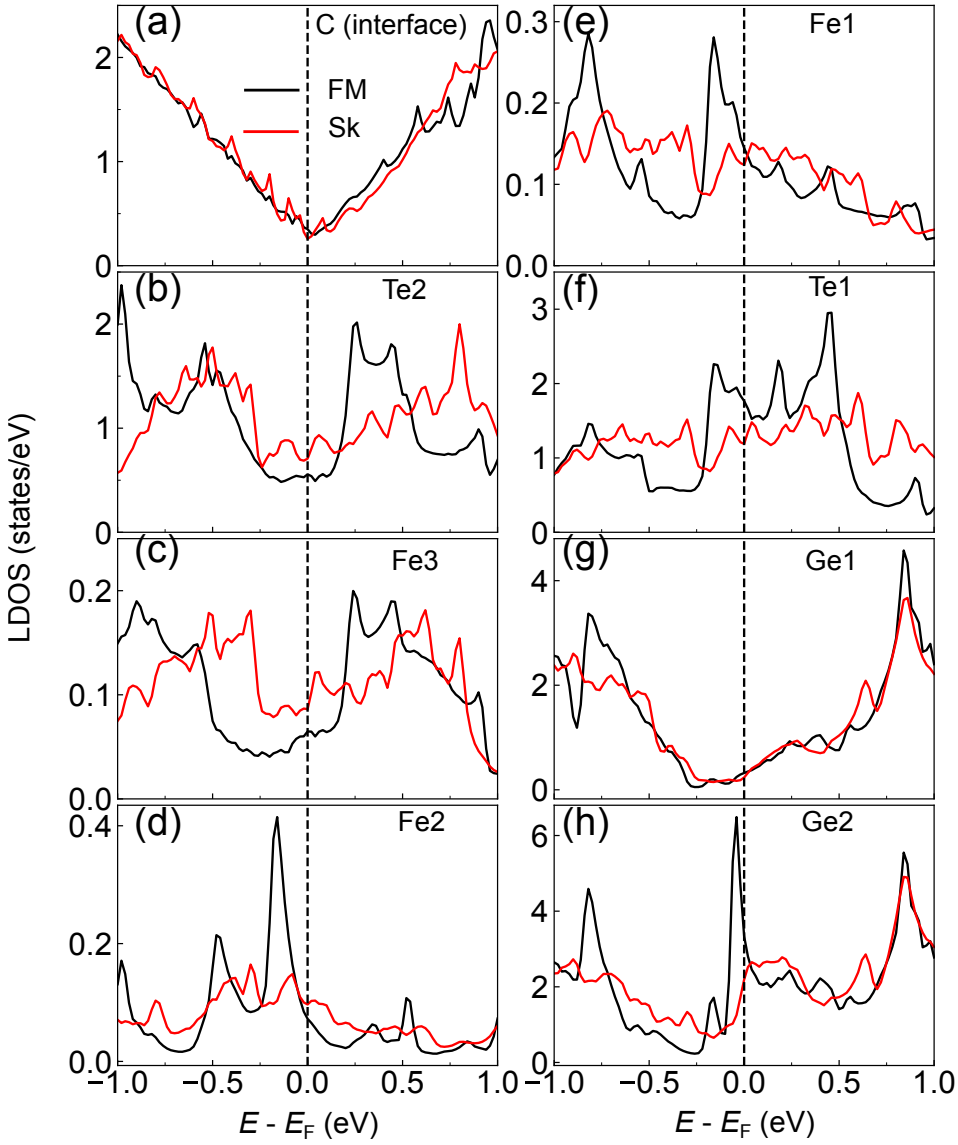

Figure S 14. LDOS of graphite/FGT/Ge/graphite tunnel device. (a) LDOS of p_z orbital character on the carbon (C) atoms at the interface between the electrode and the FGT/Ge layer in the graphite/FGT/Ge/graphite device in the FM state (black curve) and in the Sk state (red curve). (b-h) The same as in (a) but for the Te2, Fe3, Fe2, Fe1, Te1, Ge1 and Ge2 atoms, respectively (cf. sketch in Fig. 2a in the main text for atom types).

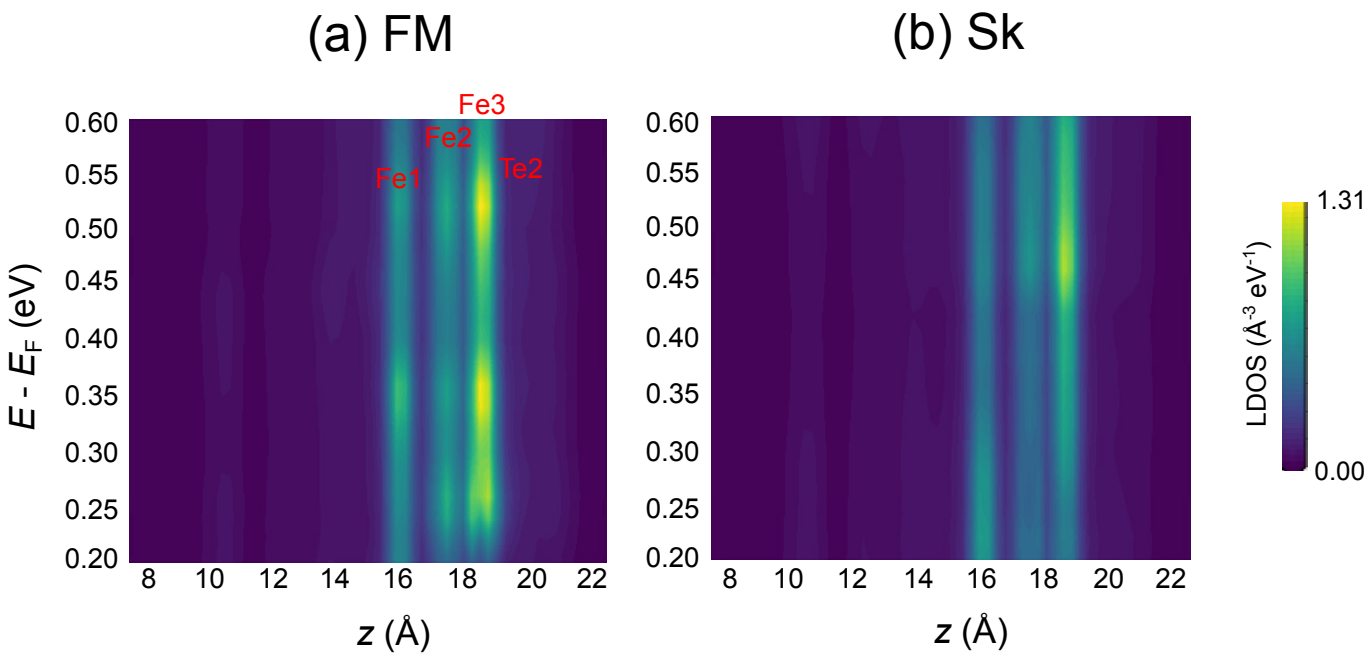

Figure S 15. LDOS map of the FM and Sk states for FGT/Ge in the energy window of [E_F+0.2, E_F+0.6] eV along the z direction (perpendicular to the surface). (a) The ferromagnetic (FM) state. (b) The skyrmion (Sk) state.

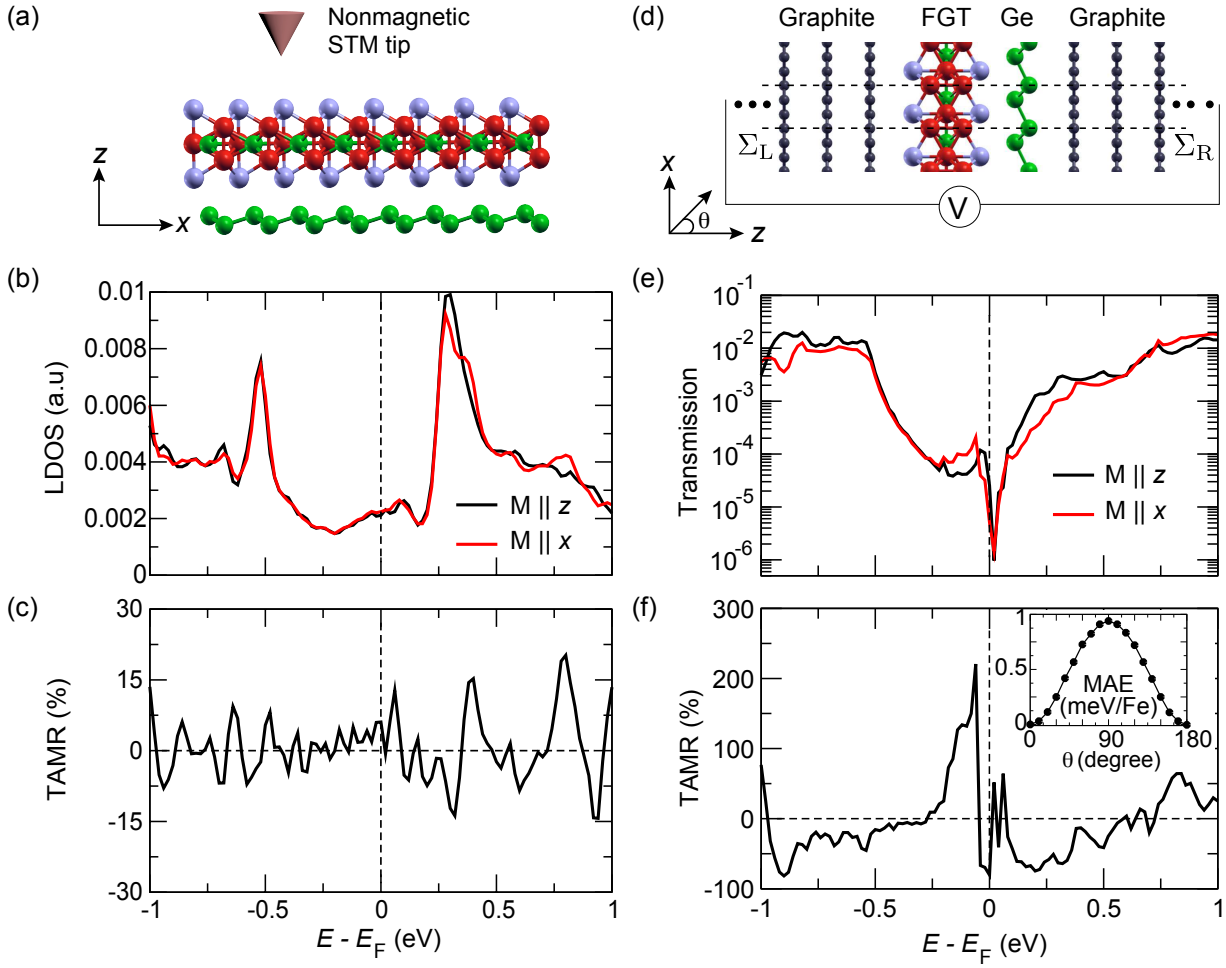

Figure S 16. Tunneling anisotropic magnetoresistance (TAMR) in STM geometry and tunnel junctions. (a) Schematic plot of an STM experiment on FGT/Ge with a non-magnetic tip. (b) Vacuum LDOS for magnetization direction along z (black) and x (red), calculated with the TH approximation. (c) Calculated TAMR, defined as TAMR $= [\mathrm{LDOS}_x(E) - \mathrm{LDOS}_z(E)]/\mathrm{LDOS}_z(E)$. (d) Side view of the atomic structure of the graphite/FGT/Ge/graphite junction. (e) Zero-bias transmission functions $T_x(E)$ and $T_z(E)$ calculated via NEGF, including SOC for the FM state with a magnetization perpendicular, $M \parallel z$ (black), and parallel, $M \parallel x$ (red), to the current flow. (f) Calculated TAMR, defined as TAMR $= [T_x(E) - T_z(E)]/T_z(E)$, where $T_x(E)$ and $T_z(E)$ are the transmission functions shown in panel (d). The inset shows the plot of the calculated magnetocrystalline anisotropy energy (MAE) arising from rotating the spin axis from the easy axis z, where θ refers to the angle between the z-axis and the magnetization direction.

Supplementary References

[1] S. Grimme, J. Antony, S. Ehrlich, and H. Krieg, A consistent and accurate ab initio parametrization of density functional dispersion correction (DFT-D) for the 94 elements H-Pu, J. Chem. Phys. **132**, 154104 (2010).

[2] Welcome to the FLEUR-project, www.flapw.de (accessed Sept. 1, 2022).

[3] P. Kurz, F. Förster, L. Nordström, G. Bihlmayer, and S. Blügel, Ab initio treatment of noncollinear magnets with the full-potential linearized augmented plane wave method, Phys. Rev. B **69**, 024415 (2004).

[4] S. Smidstrup, T. Markussen, P. Vancraeyveld, J. Wellendorff, J. Schneider, T. Gunst, B. Verstichel, D. Stradi, P. A. Khomyakov, U. G. Vej-Hansen, M.-E. Lee, S. T. Chill, F. Rasmussen, G. Penazzi, F. Corsetti, A. Ojanperä, K. Jensen, M. L. N. Palsgaard, U. Martinez, A. Blom, M. Brandbyge, and K. Stokbro, QuantumATK: an integrated platform of electronic and atomic-scale modelling tools, J. Phys. Condens. Matter **32**, 015901 (2019).

[5] D. Li, S. Haldar, T. Drevelow, and S. Heinze, Tuning the magnetic interactions in van der Waals $\mathrm{Fe_3GeTe_2}$ heterostructures: A comparative study of ab initio methods, Phys. Rev. B **107**, 104428 (2023).

[6] D. Li, S. Haldar, and S. Heinze, Strain-driven zero-field near-10 nm skyrmions in two-dimensional van der Waals heterostructures, Nano Lett. **22**, 7706 (2022).

[7] M. Perini, S. Meyer, A. Kubetzka, R. Wiesendanger, S. Heinze, and K. von Bergmann, Electrical detection of domain walls and skyrmions in Co films using noncollinear magnetoresistance, Phys. Rev. Lett. **123**, 237205 (2019).

[8] P. Giannozzi, S. Baroni, N. Bonini, M. Calandra, R. Car, C. Cavazzoni, D. Ceresoli, G. L. Chiarotti, M. Cococcioni, I. Dabo, A. D. Corso, S. de Gironcoli, S. Fabris, G. Fratesi, R. Gebauer, U. Gerstmann, C. Gougoussis, A. Kokalj, M. Lazzeri, L. Martin-Samos, N. Marzari, F. Mauri, R. Mazzarello, S. Paolini, A. Pasquarello, L. Paulatto, C. Sbraccia, S. Scandolo, G. Sclauzero, A. P. Seitsonen, A. Smogunov, P. Umari, and R. M. Wentzcovitch, QUANTUM ESPRESSO: a modular and open-source software project for quantum simulations of materials, Journal of Physics: Condensed Matter **21**, 395502 (2009).

[9] M. Bode, S. Heinze, A. Kubetzka, O. Pietzsch, X. Nie, G. Bihlmayer, S. Blügel, and R. Wiesendanger, Magnetization-direction-dependent local electronic structure probed by scanning tunneling spectroscopy, Phys. Rev. Lett. **89**, 237205 (2002).

[10] K. von Bergmann, M. Menzel, D. Serrate, Y. Yoshida, S. Schröder, P. Ferriani, A. Kubetzka, R. Wiesendanger, and S. Heinze, Tunneling anisotropic magnetoresistance on the atomic scale, Phys. Rev. B **86**, 134422 (2012).

[11] D. M. Crum, M. Bouhassoune, J. Bouaziz, B. Schweflinghaus, S. Blügel, and S. Lounis, Perpendicular reading of single confined magnetic skyrmions, Nat. Commun. **6**, 8541 (2015).

[12] A. Kubetzka, C. Hanneken, R. Wiesendanger, and K. von Bergmann, Impact of the skyrmion spin texture on magnetoresistance, Phys. Rev. B **95**, 104433 (2017).

[13] J. F. Schäfer-Richarz, P. Risius, M. Czerner, and C. Heiliger, Magnetic tunnel junctions: An efficient way for electrical skyrmion detection investigated by ab initio theory, Phys. Rev. B **100**, 214413 (2019).

[14] J.-J. Li, M.-L. Bai, Z.-B. Chen, X.-S. Zhou, Z. Shi, M. Zhang, S.-Y. Ding, S.-M. Hou, W. Schwarzacher, R. J. Nichols, *et al.*, Giant single-molecule anisotropic magnetoresistance at room temperature, J. Am. Chem. Soc. **137**, 5923 (2015).

[15] D. Rakhmilevitch, S. Sarkar, O. Bitton, L. Kronik, and O. Tal, Enhanced magnetoresistance in molecular junctions by geometrical optimization of spin-selective orbital hybridization, Nano Lett. **16**, 1741 (2016).

[16] D. Li, F. Pauly, and A. Smogunov, Giant anisotropic magnetoresistance through a tilted molecular π-orbital, Phys. Rev. Res. **2**, 033184 (2020).